SANDIA REPORT

SAND2008-7603
Unlimited Release
Printed November, 2008

Computational and Experimental Study of Nanoporous Membranes for Water Desalination and Decontamination

Bert J. Debusschere, Michael A. Hickner, Frank J. Zendejas, Helgi Adalsteinsson, Huu M. Tran, Kevin R. Long, Habib N. Najm, Douglas A. Chinn, Michael S. Kent, Blake A. Simmons

Prepared by
Sandia National Laboratories
Albuquerque, New Mexico 87185 and Livermore, California 94550

Sandia is a multiprogram laboratory operated by Sandia Corporation,
a Lockheed Martin Company, for the United States Department of Energy's
National Nuclear Security Administration under Contract DE-AC04-94-AL85000.

Approved for public release; further dissemination unlimited.

Sandia National Laboratories

Issued by Sandia National Laboratories, operated for the United States Department of Energy by Sandia Corporation.

NOTICE: This report was prepared as an account of work sponsored by an agency of the United States Government. Neither the United States Government, nor any agency thereof, nor any of their employees, nor any of their contractors, subcontractors, or their employees, make any warranty, express or implied, or assume any legal liability or responsibility for the accuracy, completeness, or usefulness of any information, apparatus, product, or process disclosed, or represent that its use would not infringe privately owned rights. Reference herein to any specific commercial product, process, or service by trade name, trademark, manufacturer, or otherwise, does not necessarily constitute or imply its endorsement, recommendation, or favoring by the United States Government, any agency thereof, or any of their contractors or subcontractors. The views and opinions expressed herein do not necessarily state or reflect those of the United States Government, any agency thereof, or any of their contractors.

Printed in the United States of America. This report has been reproduced directly from the best available copy.

Available to DOE and DOE contractors from
U.S. Department of Energy
Office of Scientific and Technical Information
P.O. Box 62
Oak Ridge, TN 37831

Telephone: (865) 576-8401
Facsimile: (865) 576-5728
E-Mail: reports@adonis.osti.gov
Online ordering: http://www.osti.gov/bridge

Available to the public from
U.S. Department of Commerce
National Technical Information Service
5285 Port Royal Rd
Springfield, VA 22161

Telephone: (800) 553-6847
Facsimile: (703) 605-6900
E-Mail: orders@ntis.fedworld.gov
Online ordering: http://www.ntis.gov/help/ordermethods.asp?loc=7-4-0#online

SAND2008-7603
Unlimited Release
Printed November, 2008

Computational and Experimental Study of Nanoporous Membranes for Water Desalination and Decontamination

Bert J. Debusschere and Habib N. Najm
Reacting Flow Research Department

Helgi Adalsteinsson
Scalable Computing R&D Department

Frank J. Zendejas, Huu M. Tran, and Blake A. Simmons
Energy Systems Department
P.O. Box 969
Livermore, CA 94551-0969

Douglas A. Chinn
Advanced Prototyping S&T Department

Michael S. Kent
Biomolecular Analysis & Imaging Department
P.O. Box 5800
Albuquerque, NM 87185

Michael A. Hickner
Penn State University
University Park, PA 16802

Kevin R. Long
Texas Tech University
Lubbock, TX 79409-1042

Abstract

Fundamentals of ion transport in nanopores were studied through a joint experimental and computational effort. The study evaluated both nanoporous polymer membranes and track-etched nanoporous polycarbonate membranes. The track-etched membranes provide a geometrically well characterized platform, while the polymer membranes are are more closely related to ion exchange systems currently deployed in RO and ED applications. The experimental effort explored transport properties of the different membrane materials. Poly(aniline) membranes showed that flux could be controlled by templating with molecules of defined size. Track-etched polycarbonate membranes were modified using oxygen plasma treatments, UV-ozone exposure, and UV-ozone with thermal grafting, providing an avenue to functionalized membranes, increased wettability, and improved surface characteristic lifetimes. The modeling effort resulted in a novel multiphysics multiscale simulation model for field-driven transport in nanopores [2]. This model was applied to a parametric study of the effects of pore charge and field strength on ion transport and charge exclusion in a nanopore representative of a track-eteched polycarbonate membrane.

The goal of this research was to uncover the factors that control the flux of ions through a nanoporous material and to develop tools and capabilities for further studies. Continuation studies will build toward more specific applications, such as polymers with attached sulfonate groups, and complex modeling methods and geometries.

Contents

1 Introduction **11**

2 Membrane Synthesis and Modification Methods **15**

Track-Etched Membrane surface modification 15

Polyaniline Irregular Pore Membrane Synthesis 16

3 Membrane Characterization Methods **19**

Measurement of zeta potential 19

NaCl transport 19

Microscopy of Membrane Surfaces 21

4 Simulation Model **23**

Problem Definition 23

Continuum Model 23

Formulation 24

Finite element PNP model 25

Weak electrostatic equations 26

Weak transport equations 26

Implementation 27

Particle-Based Model 27

Formulation 27

Implementation 29

Multiscale Coupling 30

Introduction 30
Multiscale formulation 30
Implementation 32

5 Results and Discussion **35**
Membrane Characterization 35
Track-Etched Membrane Contact Angle Measurements 35
Track-Etched Membrane Surface Characterization 35
Track-Etched Membrane Surface Charge 37
Membrane Transport Properties 38
Measurements 38
Polyaniline Membrane Transport 38
Track-Etched Membrane Transport Properties 41
Simulations 42

6 Conclusions **53**

References **54**

List of Figures

1.1 A schematic of an electrodialysis stack. Negatively charged ions and membranes are shown in red, positively charged ions and membranes are shown in blue. 12

2.1 SEM micrograph of a native PCTE membrane. 15

2.2 Monomers selected for the thermal grafting copolymerization surface modification of PCTE membranes. 16

2.3 Molecular doping mechanism and doping schematic for poly(aniline) membranes. 17

2.4 Scanning electron cross-sectional micrographs of dense poly(anline) 1.6 micron thick membranes supported on porous substrates. 18

3.1 Schematic of streaming current measurement to compute zeta potential and example of raw data showing linear relationship between streaming current and pressure drop. 20

3.2 Experimental set-up for diffusion measurements and representative data showing the increase in salt concentration as a function of diffusion time. 20

3.3 Experimental apparatus for potential-driven flux measurements. 21

3.4 Raw data for potential flux experiments showing current trace as a function of time and the resulting linear current voltage relationship used to calculate the membrane resistance. 22

4.1 Membrane and pore geometry: cross section of membrane with cylindrical pores (left). A control volume around one of the pores forms the computational domain for the single-pore multiscale model in this work (right). Ions are driven through the pore by a combined applied concentration and potential gradient. Different models are used in the different sections of the domain: I: Continuum, II: Particle-Based. 24

4.2 Flow chart for multiscale electrodesalination simulations. 32

4.3 Schematic management of a multiscale simulation on 32 nodes with MPI-unaware continuum simulations and four replicate BD simulations. The rows in this table represent successive steps in the program execution. The colums represent the nodes on which the steps are executed. 33

5.1 SEM micrograph of a PCTE membrane damaged by a 60 minute UV-ozone exposure. 36

5.2 SEM micrograph of a PCTE membrane exposed to UV-ozone for 15 minutes, with subsequent 5 minute thermal graft of 1.0 wt % AAc. 36

5.3 Contact angle comparison of thermally grafted monomers verses an un-modified PCTE membrane. The data represents contact angles taken for two week old membranes. 37

5.4 Surface features of an unmodified PCTE membrane. 38

5.5 Front and back comparison of membranes grafted with various monomers: (a) and (b) correspond to the front and back sides of a membrane grafted in 1 wt % acrylic acid solution. (c) and (d) correspond to the front and back sides of a membrane that was grafted in 1 % dimethylacrylamide solutions. (e) and (f) are the front and back sides of a membrane that was grafted in 1 % Dimethylaminoethyl methacrylate solution. 39

5.6 Schematic of pore cross section showing grafted membrane surface. 40

5.7 Computed zeta potential of modified PCTE membranes as a function of pH. . 40

5.8 Small-angle neutron scattering curves for as cast and undoped membranes immersed in D2O. 41

5.9 Glucose diffusion as a function of doping ratio in PANI membranes. 42

5.10 Comparison of modified PCTE membranes showing relationship of potential-driven and diffusive fluxes to zeta potential. 43

5.11 Computational domain 43

5.12 Convergence of ion concentrations and fluxes with PNP/BD iteration count for a case with an applied potential of 0.2 V, c_1 = 150 mM, c_2 = 050 mM, and a wall charge inside the pore of +0.1 C/m^2 44

5.13 Sodium (top) and chloride (bottom) concentration fields in electrodialysis through a negatively charged pore through a membrane. An axial cross section of the pore is shown in the center, in between a continuum species transport zone upstream and downstream. The membrane material surrounding the pore is not shown. Black dotted lines indicate the location of the handshake region between the continuum and BD models. 45

5.14 Solution charge density (represented as signed electrolyte concentration) in electrodialysis through a negatively charged nanoporous desalination membrane. 45

5.15 Fluxes for 0.2V, c_1 = 150 mM, c_2 = 150 mM 46

5.16 Fluxes for c_1 = 150 mM, c_2 = 050 mM 47

5.17 Total currents as a function of wall charge inside pore. 47

5.18 [Na^+] from sampled BD fields for case of 0.2V, c_1 = 150 mM, c_2 = 050 mM as a function of the wall charge inside the pore. The wall charge was varied from -0.1 C/m^2 (top panel) to 0.2 C/m^2 (bottom panel) in 0.05 C/m^2 increments. . 49

5.19 [Cl^-] from sampled BD fields for case of 0.2V, c_1 = 150 mM, c_2 = 050 mM as a function of the wall charge inside the pore. The wall charge was varied from -0.1 C/m^2 (top panel) to 0.2 C/m^2 (bottom panel) in 0.05 C/m^2 increments. . 50

5.20 Bulk charge concentration from sampled BD fields for case of 0.2V, c_1 = 150 mM, c_2 = 050 mM as a function of the wall charge inside the pore. The wall charge was varied from -0.1 C/m^2 (top panel) to 0.2 C/m^2 (bottom panel) in 0.05 C/m^2 increments. 51

List of Tables

2.1 Possible strong-acid poly(aniline) dopants and their anticipated pore size and porosity as a function of dopant level. 18

Chapter 1

Introduction

Membrane-based desalination is a mature and efficient technology for extracting fresh water from salty or otherwise impaired sources. The dominant technology is reverse osmosis (RO), but electrodialysis (ED) has become an efficient alternative for purifying slightly impaired water [40]. The ED method relies on electrophoretic transport of solute ions from a diluate (source) stream through ion exchange membranes and into a concentrate (sink) stream. This approach, thus, differs from reverse osmosis and thermal desalination methods in that solute ions are removed from a water stream, rather than the other way around, and that only ionic solutes are removed from the source stream. These characteristics facilitate the design of flow-through electrodialysis systems (shown schematically in Figure 1.1), can help reduce the effects of fouling and clogging of desalination membranes, but have also largely limited the application of these methods to water sources with low salinity or in specialized deployment areas [58].

Novel membranes that increase water flux are one of the principal routes to advancing water treatment technology [43]. Since there is no single glaring limitation in membrane-based desalination processes, improvements must come from a combination of overall throughput, membrane stability, and ionic selectivity. Achieving progress in these areas requires improved understanding of the physical processes involved in transport through the membranes [40]. Another compelling reason for seeking more detailed insight and rational membrane design capabilities is to achieve selective electrodialysis, which is a relatively recent approach to treatment of marginally impaired water. In selective electrodialysis, the ion exchange membranes are chosen such that they facilitate transport of specific target ions more than those of common, non-toxic ionic solutes. Since the amount of ions transported across the ion exchange membrane is now only a fraction of the overall salt concentration in the source stream, these systems are expected to achieve substantially higher energy efficiency than reducing the concentrations of all ionic solutes to levels dictated by the least desirable species [3].

Porous membranes that respond to pH [65, 61, 30], temperature [31, 46], or ionic strength [65, 30], have repeatedly been the focus of research over past decades. A major reason for the continued interest in stimuli-responsive porous membranes is due to applications in diverse fields such as desalination of water [5, 6], separation of salts by reverse osmosis [64, 41], ultra- and micro-filtration [19, 10], and their potential use as biological separation membranes [14]. Most commercial membranes used for these applications are polymers with favorable chemical and thermal-mechanical bulk properties. Often, however, these same polymers chosen

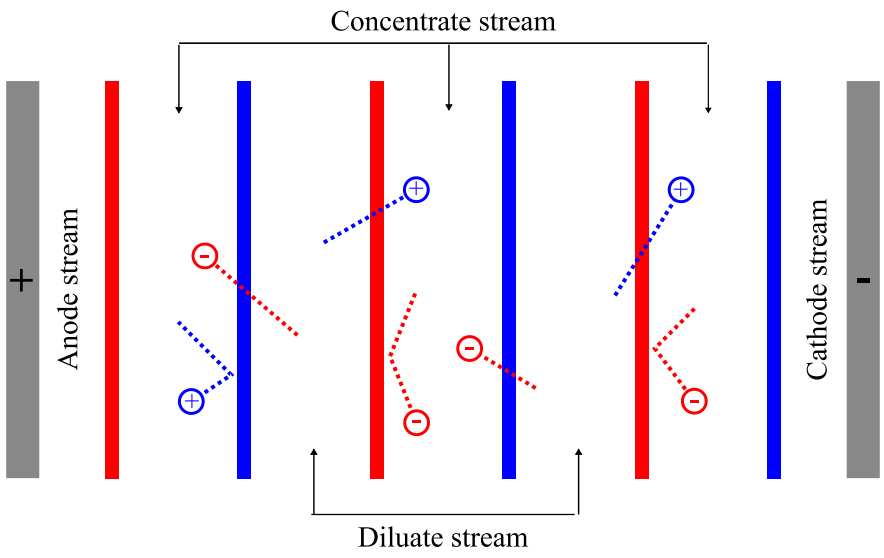

Figure 1.1. A schematic of an electrodialysis stack. Negatively charged ions and membranes are shown in red, positively charged ions and membranes are shown in blue.

due to their bulk properties are hydrophobic; and result in surface properties that are undesirable and make the membranes less optimal for the intended application. For example, research has demonstrated that hydrophobic membranes are more susceptible to fouling than hydrophilic membranes [57, 49]. Fortunately, there are surface modifying techniques that modify the surface properties of the substrate without changing the properties of the bulk material. Early surface modification methods of polymer membranes included oxidative techniques such as: plasma treatments [33, 56, 59], corona discharge treatments [51, 34], and ultra violet light exposure [28, 21, 44]. Selection of a specific surface modification technique depends on the chemical structure of the given support membrane and the desired characteristics of the surface modification required. Although these techniques have proven to be extremely simple, they do not impart permanent hydrophilicity to the membrane due to the limited stability of the treated surface towards washing and storage.

More complex and advanced technologies, such as surface grafting, and coating polymerization are being used to modify the surface properties of membranes. Among these methods, graft polymerization is one of the most efficient methods to control the polar monomer adsorbed onto the membrane surface and to durably modify the membrane surface properties. Surface graft polymerization has attracted considerable interest as a simple and versatile approach to introduce functional groups onto a variety of polymeric substrates. In graft polymerization, active sites are first introduced on the membrane surface using the same techniques described earlier such as plasma treatment, glow-discharge, ozone treatment, or UV-ozone irradiation. However, the membranes undergo a subsequent monomer polymerization step where adsorption of soluble polymer from solution grafts onto the active sites.

This process provides a more robust functionalization of the grafted polymer chains since they are chemically bonded between the substrate and polymer [13, 8, 63].

Studies of ED through some synthetic nanoporous membranes have shown ionic selectivity and conductance properties similar to those of biological ion channels [55, 11]. This raises the possibility of achieving improved purification systems for impaired water by controlling the ionic selectivity of the membrane system [3]. The transport involves multiple different length scales, ranging from ion sizes, through the Debye length and nanopore radius, and up to concentration polarization effects on a device level. The timescales involved are equally diverse, ranging from sub-picosecond timescales for atomic motions to minutes for concentration evolution. Simulations of ion channels have been tackled with a corresponding range of simulation methods, ranging from explicit molecular dynamics models [17, 20], through reduced-order particle models such as Brownian Dynamics [15] and continuum methods such as Poisson-Nernst-Planck [23, 12]. Each model makes a variety of assumptions and approximations regarding the nature of the simulation system, and lively debates regularly emerge over the validity of the various assumptions for a given class of simulations [36, 42, 16, 22].

While significant advances have been made in membrane technology for water treatment, most of the developments still occur on a trial-and-error basis. In order to enable a science-based membrane design capability, a detailed insight will be required into the factors controlling the flux of ions through nanoporous membranes. Through a combined experimental and computational approach, this works aims to acquire such insight and to develop the tools and capabilities required for more detailed studies and engineering of membrane materials used in electrodesalination. To achieve these goals, significantly improved insight is required into the detailed chemical and physical interactions between the ion exchange membranes, the ionic solutions, and the applied electric fields. In particular, improved understanding is needed for the effects of membrane charge and chemical composition, the influence of pore geometry and surface roughness, and non-equilibrium effects such as charge polarization. The platforms used in this study, nanoporous polymers [35], polymers modified with ions [45], and track-etched nanoporous polycarbonate membranes, were chosen to provide both a well-characterized platform for experimental and modeling studies and to provide a clear path toward desalination membranes relevant to currently deployed membrane systems.

Ion track-etched membranes are formed by first irradiating polymer materials (e.g. polycarbonate sheets) with ions, which locally damage the polymer. Subsequent etching results in a membrane with geometrically uniform, cylindrical pores at the locations where ions went through the material. This simplified geometry is a good system for studying the effects of fluid – wall interactions, decoupled from the complex geometry of more conventional nanoporous membranes. Track-etched membranes were therefore the main focus of both the experimental and computational efforts in this project. In this work, surface modifications were made to track-etched membranes in order to study their effect on the membrane characteristics and the associated ionic fluxes through the membranes. We used advanced grafting techniques to modify the surface of polycarbonate track etched membranes using oxygen plasma treatments, ultra-violet irradiation and UV-ozone exposure, and UV-ozone followed by a thermal grafting process. These advanced surface modification techniques pro-

vide an avenue to functionalize polymer membranes with various ionic monomers to create fixed-charge ion-exchange membranes. Since the surface modifications increase the wettability of the membrane, they are less susceptible to fouling, and thirdly the grafted surface modifications provide improved surface characteristic lifetimes. The modified membranes surface properties were initially characterized by monitoring the water contact angles, and subsequently by measuring the surface charge. The properties of the modified membranes were investigated experimentally for both concentration and electric field driven transport.

The poly(aniline) membranes investigated in this work had a pore network that was templated by molecules with a defined size. By adjusting the doping level, we were able to show that the pore space was indeed affected and the flux could be controlled. While it remains difficult to completely characterize the topology of the pore space in irregular pore membranes well enough to connect experimental results in both regular and irregular pore membranes, we believe the framework set forth in this project holds significant promise for advancing fundamental understanding of transport in nanoporous membranes with various surface chemistries and pore topologies.

To provide deeper insight into the key mechanisms of ion transport through the nanopores of the membranes, the experimental work was complemented with a modeling and simulation component. Given the wide range of spatial and temporal scales in electrodialysis and the non-equilibrium nature of these systems, coupled multiscale simulations were chosen as the most rigorous way to represent the chemical and physical detail needed at the membrane pores and interfaces while permitting realistic handling of long-time evolution and field-driven interactions. The most interesting properties of the system, ionic selectivity, response to chemical functionalization, and susceptibility to fouling, are all determined by very small scale interactions near the pore wall [9]; in fact, the emergence of selective transport is widely believed to happen when the channel radius becomes narrower than the Debye length (or double layer thickness), which can also be taken to be the length at which finite particle size starts to matter and continuum approximations become less appropriate. A multiscale model composed of a particle model for the confined nanopore and a continuum representation of the surrounding area should provide the best of both worlds; a detailed view of ion distributions and chemical interactions within the pore, and an efficient model for device-level transport and long-timescale system evolution [32, 27].

The overarching goal of both the experimental and computational work was to uncover the factors that control the flux of ions through a nanoporous material and develop tools and capabilities for further studies. As the work on modeling and regular pore membranes comes into agreement, the complexity of the materials can be increased to encompass membranes that may be more applicable to specific applications, such as polymers with attached sulfonate groups. More complex modeling methods and geometries may be used to test the limits of the computational approaches developed.

The next section gives an overview of the membrane synthesis and modification methods used in this work. Section 3 then covers the methods used to characterize the structural and surface properties of the resulting membranes. The modeling formulation is covered in section 4. A detailed discussion of the results is given in section 5.

Chapter 2

Membrane Synthesis and Modification Methods

Track-Etched Membrane surface modification

Commercially available track-etched membranes, purchased from Ion Track Technology for Innovative Products (Belgium), were surface modified using oxygen plasma, UV-ozone, and UV-ozone activated thermal grafting. The membranes have a 20 μm thickness, 10 nm pore diameter, and a pore density of $4.0\times10^{9}cm^{-2}$. Track-etched membranes, as shown in Fig. 2.1, were chosen for their regular, cylindrical pore structure (which facilitates comparison between the experimental and computational studies) and for the ease of polycarbonate functionalization.

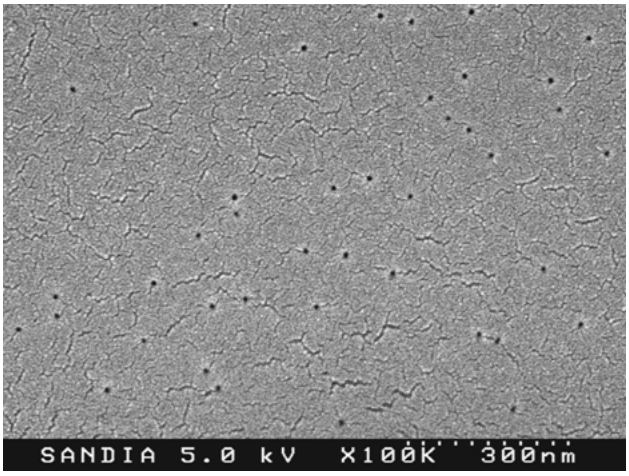

Figure 2.1. SEM micrograph of a native PCTE membrane.

We pursued three surface modifying techniques: 1) oxygen plasma, 2) UV-ozone, and 3) UV-ozone followed by thermal grafting. The oxygen-plasma treatment led to improvements in the membrane wetting properties, with water contact angle reductions from the native 70° to as low as 35°. However, it was difficult to reproduce the results without etching and

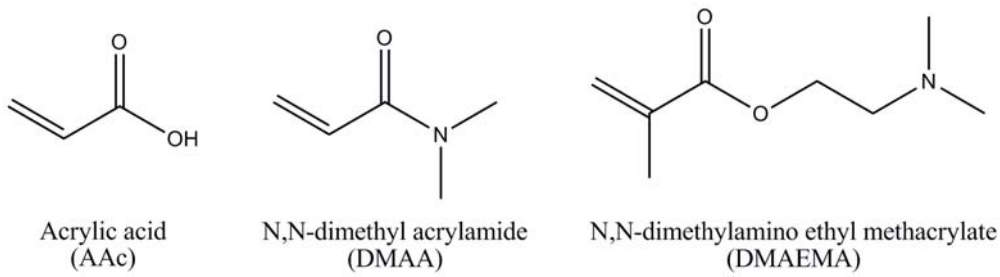

Figure 2.2. Monomers selected for the thermal grafting copolymerization surface modification of PCTE membranes.

consequently enlarging the pores. Also, the surface modifications were not stable in time. To avoid the pore etching and time-dependent effects, we tested 15, 30, and 60 min UV-ozone treatments with and without surface grafting copolymerization of the activated membrane.

The UV-ozone treatment generates peroxides and hydroxyperoxides at the surface that are capable of initiating radical polymerization of vinyl monomers, resulting in surface-grafted chains. This thermal grafting process provides a method to chemically control the surface charge properties of the membrane by choosing the proper monomer. For the current studies we investigated acrylic acid (AAc), N,N-Dimethylacrylamide (DMAA), and 2(N,N-Dimethylamino)ethyl methacrylate (DMAEMA) monomers, as shown in Fig. 2.2. The UV-activated membranes were immersed in respective monomer aqueous solutions ranging between (0.1 – 2.0 wt%) for 5, 15, and 30 minutes at 65°C. The membranes were then washed with deionized (DI) water to remove the residual un-grafted homopolymer.

Polyaniline Irregular Pore Membrane Synthesis

Irregular pore membranes were fabricated using a molecular doping approach to create materials with controlled pore size and porosity. Poly(aniline) (Panipol, Porvoo Finland) was doped with strong acids of various molecular sizes. The pore size was controlled by the molecular size of the dopant, and the total pore volume was controlled by the doping ratio, moles of acid dopant per mole of poly(aniline) (PANI) repeat unit. The molecular doping mechanism of PANI with a strong acid is shown in figure 2.3. Also shown in figure 2.3 is a schematic of how the anion size changes the average distance between PANI chains thereby creating pore space within the material.

A series of acids is shown in table 2.1 along with their calculated molecular size and anticipated porosity as a function of doping ratio. This table served as a guide for selection of dopant molecules and doping ratios to affect the desired transport properties. In a general preparation, 0.25 g of PANI was dissolved in 20 mL of formic acid. The desired amount of dopant was dissolved in approximately 5 mL of formic acid. After total dissolution of both

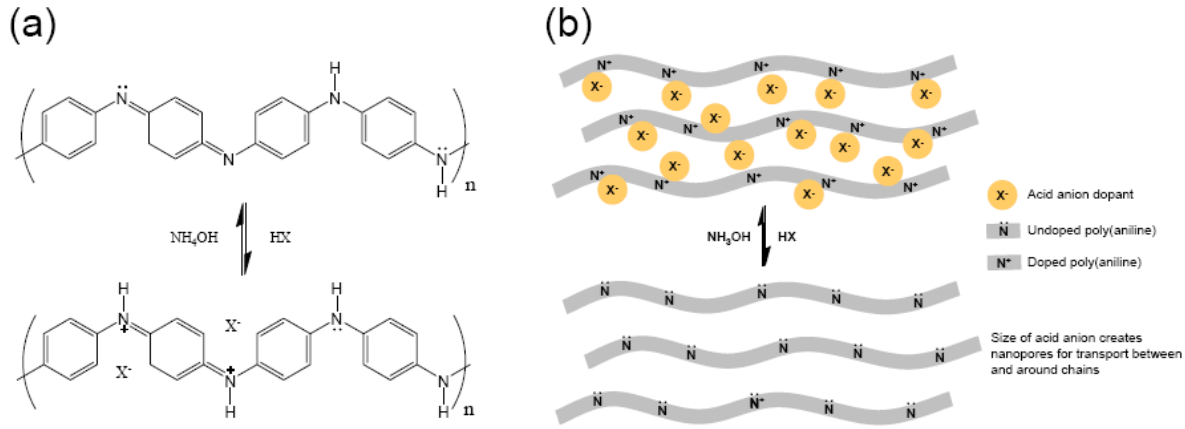

Figure 2.3. Molecular doping mechanism and doping schematic for poly(aniline) membranes.

PANI and acid (approximately 5 hours), the two solutions were combined and left to stir for at least 12 hours. Longer stirring times before casting between 24 and 72 hours often yielded higher-quality films.

In order to obtain membrane in thin-film format, the doped PANI membranes were spun cast onto porous poly(sulfone) support membranes (avg. pore size 0.22 μm) (Sterlitech, Kent WA. A porous support was affixed to a silicon wafer using a silicone rubber gasket. The gasketed porous support membrane was then spun at 2000 RPM. Approximately 2 mL of hexane was dispensed onto the porous support to completely wet the substrate and fill the pores. The doped PANI solution in formic acid was then dispensed onto the hexane-filled membrane and allowed to dry under spinning, about 2 min. The resulting asymmetric membranes were characterized for active layer thickness by cryo fracturing under liquid nitrogen and examining the fracture surface by FESEM. Figure 2.4 shows the cross section of a typical membrane. The thickness of the active layer could be controlled by the spinning speed and PANI solution concentration. Dry membranes were equilibrated in DI water before measurement or dedoped in 0.1 M NaOH and then rinsed and equilibrated in DI water before measurement.

	Molecular diameter* (nm)	Molar doping ratio dopant:PANI 1:0.5	1:1	1:2
		Porosity (vol %)		
MSA	0.59	10	18	30
ESA	0.63	12	21	35
TSA	0.74	18	30	46
CSA	0.82	23	37	54
DBSA	1.0	34	51	68

MSA = methanesulfonic acid
ESA = ethanesulfonic acid
TSA = toluenesulfonic acid
CSA = camphorsulfonic acid
DBSA = dodecylbenzenesulfonic acid
* Molecular diameters from calculated molar volumes using Advanced Chemistry Development (ACD/Labs) Software V8.14 for Solaris © 1994-2007 ACD/Labs

Table 2.1. Possible strong-acid poly(aniline) dopants and their anticipated pore size and porosity as a function of dopant level.

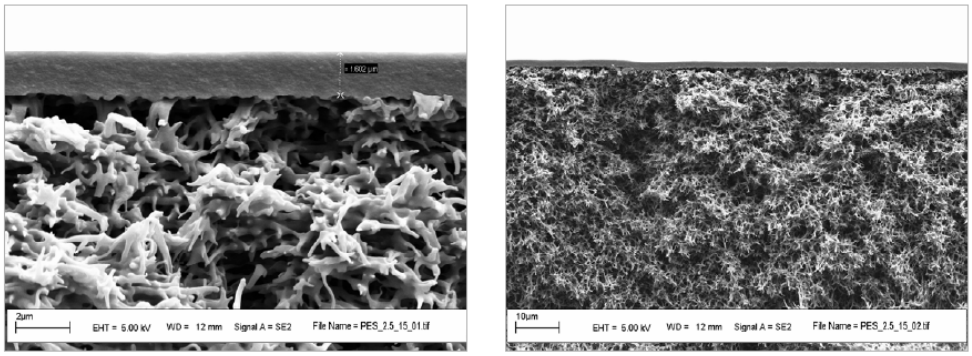

Figure 2.4. Scanning electron cross-sectional micrographs of dense poly(anline) 1.6 micron thick membranes supported on porous substrates.

Chapter 3

Membrane Characterization Methods

Measurement of zeta potential

A SurPASS (Anton Paar GmbH, Graz, Austria) electrokinetic analyzer was used to measure the zeta potential of the poly (acrylic acid) grafted PCTE membranes across a range of pH values [39]. A 0.001 M KCl solution was used as the electrolyte and HCl (0.1 M) and NaOH (0.1 M) were used to adjust the pH. The zeta potential (ζ) of the grafted surface was computed from measured streaming current and the measured dimensions of the flow cell using the Helmholtz-Smoluchowski equation:

$$\zeta = \frac{dI}{dp} \cdot \frac{\eta}{\epsilon\epsilon_0} \cdot \frac{L}{A} \tag{3.1}$$

where dI/dp is the slope of streaming current versus pressure curve, η is the electrolyte dynamic viscosity, ϵ_0 is the vacuum permittivity, ϵ is the dielectric constant of the electrolyte, L is the length of the streaming channel and A is the cross-sectional area of the streaming channel. A schematic of the membrane slit geometry for the measurements and an example of the data is shown in Figure 3.1.

NaCl transport

The permeation of NaCl through PCTE membranes was carried out at 30°C, using a 0.15M NaCl concentration gradient. The NaCl concentration change during permeation measurements was monitored using a refractive index detector (Waters 2414). The permeability of the membrane was computed using a standard analysis for a membrane separated diffusion cell [18]. A schematic of the membrane separated cell used for both NaCl and glucose transport and an example of the data is shown in Figure 3.2.

The potential driven current through the PCTE membranes was measured using a Solartron 1286 electrochemical interface, using 0.15M NaCl on both sides of the membranes as electrolyte. Ag/AgCl wire electrodes were placed on each side of the membrane to sense the potential drop across the membrane and platinum mesh electrodes were placed 1.5 cm from the surface of the membrane to drive the ionic current as shown in Figure 3.3. Current versus

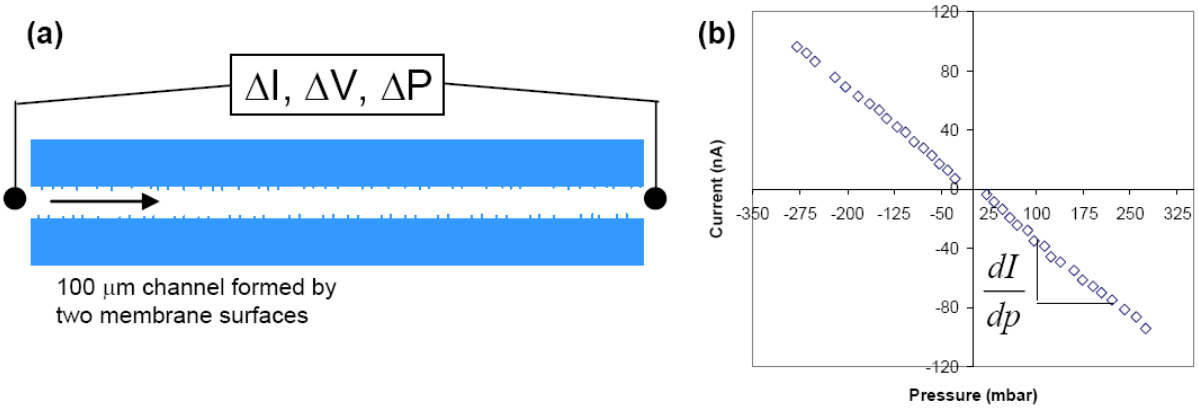

Figure 3.1. Schematic of streaming current measurement to compute zeta potential and example of raw data showing linear relationship between streaming current and pressure drop.

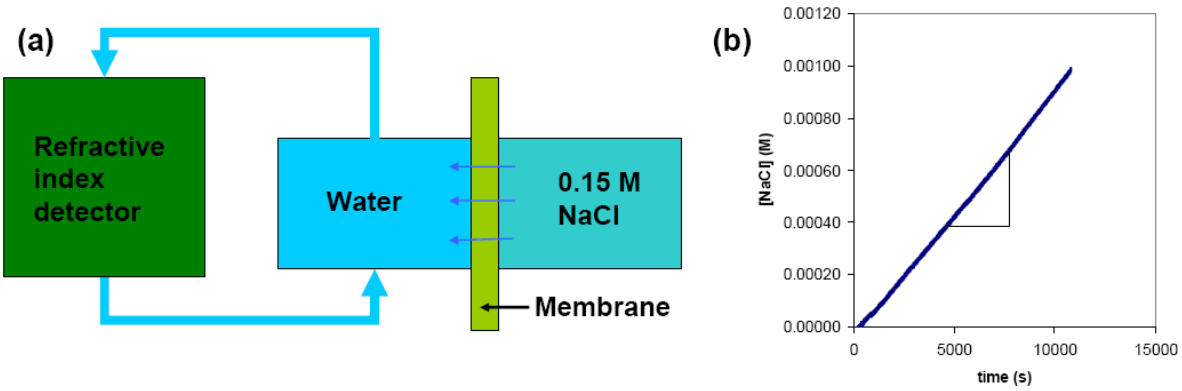

Figure 3.2. Experimental set-up for diffusion measurements and representative data showing the increase in salt concentration as a function of diffusion time.

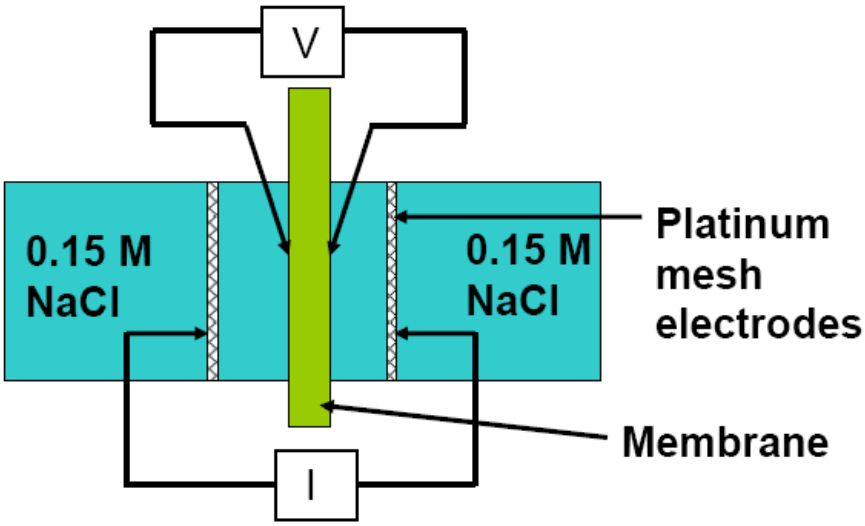

Figure 3.3. Experimental apparatus for potential-driven flux measurements.

time plots were recorded at +/- 50, 100, 200, and 300 mV across the Ag/AgCl electrodes. Note that during the experiments, the voltage was reversed on a regular basis in order to avoid excessive changes in the ion concentrations on both sides of the membrane. A current versus potential plot could then be constructed with the resistance of the membrane being the slope of the curve as shown in Figure 3.4. The resistance of the open cell was subtracted from the membrane measurements to compute the final ionic transport resistance of the membrane.

Microscopy of Membrane Surfaces

For inspection of the membrane surfaces, before and after modifications, field emission scanning electron micrographs were acquired of membrane surfaces with a JEOL 6700F instrument at 10 kV acceleration voltage. Before imaging, the membrane surfaces were first coated with a sub 4 nm layer of iridium metal.

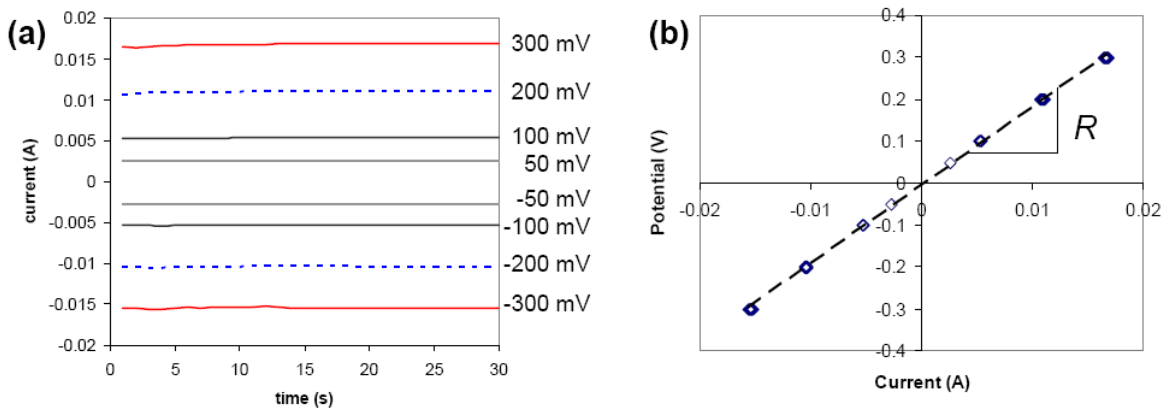

Figure 3.4. Raw data for potential flux experiments showing current trace as a function of time and the resulting linear current voltage relationship used to calculate the membrane resistance.

Chapter 4

Simulation Model

Problem Definition

To study ionic flux through nanoporous membranes, we consider a membrane containing cylindrical pores normal to the membrane surface, as depicted in the cross-section on the left side of Fig. 4.1. While this geometry would be a gross over-simplication of the tortuous path nanoporous membranes that are commonly used in industrial water treatment applications, it is representative of the structure of ion track-etched membranes.

The computational domain for a single-pore simulation is shown on the right side of Fig. 4.1. It shows a single pore through the membrane (hashed section) in the center. The computational domain also includes an entrance and exit section that extend several pore diameters away from the pore. Ions are transported through the pore by an applied potential and/or concentration gradient. The transport in zone I, a little distance away from the pore, can be modeled using a continuum representation. In zone II, however, inside the pore and near the pore entrance and exit, particle-based representations are more appropriate to account for finite ion sizes as well as ion-ion and ion-wall interactions. Information between the models in zones I and II is exchanged at the surface separating them. While a 3D particle model is used in zone II, the continuum model uses an axisymmetric 2D formulation. If the continuum domain is wide enough in the radial direction, we can assume that ions only enter the domain through the planes parallel to the membrane, allowing the use of no-flux boundary conditions on the edges of the computational domain in the radial direction. The various models for the ionic transport are explained in more detail in the following sections.

Continuum Model

In the areas of the computational domain where continuum assumptions hold, namely that the flow length scales are sufficiently large with respect to molecular length scales, species transport is modeled by the Poisson-Nernst-Planck (PNP) equations [48]. Bulk flow is assumed to be negligible given the large flow-area change in going through the membrane pores, so the bulk velocity field is set to zero and the momentum equation is not solved. The sections below describe the PNP equations, their non-dimensionalization and their implementation.

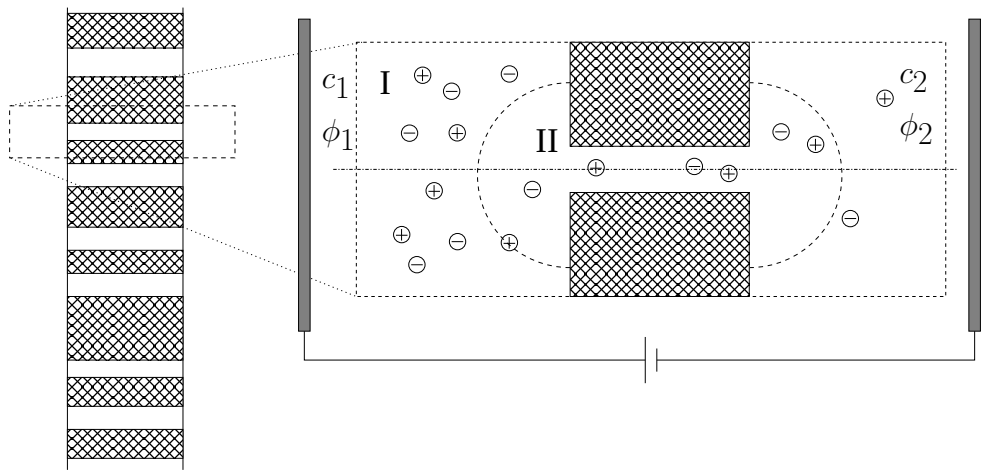

Figure 4.1. Membrane and pore geometry: cross section of membrane with cylindrical pores (left). A control volume around one of the pores forms the computational domain for the single-pore multiscale model in this work (right). Ions are driven through the pore by a combined applied concentration and potential gradient. Different models are used in the different sections of the domain: I: Continuum, II: Particle-Based.

Formulation

The PNP equations consist of a transport equation for the species concentrations c_i:

$$\frac{\partial c_i}{\partial t} + \nabla \cdot [c_i(\boldsymbol{u} + \boldsymbol{u}_i^e)] = \nabla \cdot (D_i \nabla c_i) \tag{4.1}$$

coupled with the Maxwell equation for the electric potential ϕ:

$$\nabla \cdot (\epsilon \nabla \phi) = -\rho_e - \rho_p \tag{4.2}$$

In these equations, D_i is the diffusion coefficient, $\boldsymbol{u}$ is the convective velocity field, and $\boldsymbol{u}_i^e$ is the electrophoretic velocity of species i, obtained from

$$\boldsymbol{u}_i^e = -\beta_i z_i F \nabla \phi \tag{4.3}$$

where z_i is the valence, F is the Faraday constant, and β_i is the electrophoretic mobility, related to the diffusion coefficient through the Nernst-Einstein equation: $D_i = RT\beta_i$, with R the universal gas constant and T the absolute temperature. In equation (4.2), ρ_e is the ionic charge density in the solution, computed as $\rho_e = F \sum_i z_i c_i$, ρ_p is the density of fixed charges (e.g. on the membrane), and ϵ is the electrical permittivity of the medium.

To non-dimensionalize these governing equations, we choose a reference concentration, length, diffusion coefficient and temperature:

$$
\begin{aligned}
c_{\text{ref}} &= 1 \text{ mol/m}^3 && (4.4)\\
L_{\text{ref}} &= 10^{-9} \text{ m} && (4.5)\\
D_{\text{ref}} &= 10^{-9} \text{ m}^2\text{/s} && (4.6)\\
T_{\text{ref}} &= 298 \text{ K} && (4.7)
\end{aligned}
$$

from which the following reference quantities can be derived:

$$
\begin{aligned}
\phi_{\text{ref}} &= \frac{F c_{\text{ref}} L_{\text{ref}}^2}{\epsilon_0} = 1.09 \times 10^{-2} \text{ V} && (4.8)\\
u_{\text{ref}} &= \frac{D_{\text{ref}}}{R T_{\text{ref}}} F \frac{\phi_{\text{ref}}}{L_{\text{ref}}} = 0.424 \text{ m/s} && (4.9)\\
\tau_{\text{ref}} &= \frac{L_{\text{ref}}}{u_{\text{ref}}} = 2.36 \times 10^{-9} \text{ s} && (4.10)\\
Pe_{\text{ref}} &= \frac{u_{\text{ref}} L_{\text{ref}}}{D_{\text{ref}}} && (4.11)\\
\rho_{\text{ref}} &= F c_{\text{ref}} && (4.12)
\end{aligned}
$$

where we have used the vacuum permittivity $\epsilon_0 = 8.85 \times 10^{12}$ F/m as the reference electrical permittivity.

By substituting each dimensional variable in equation (4.1) by its corresponding non-dimensional variable multiplied by its associated reference quantity, and, for convenience, reusing the same nomenclature for the non-dimensional variables in the rest of the document, we obtain the following set of non-dimensionalized equations:

$$
\begin{aligned}
\frac{\partial c_i}{\partial t} + \nabla(\boldsymbol{u} c_i) - \nabla[(D_i z_i \nabla \phi) c_i] &= \frac{1}{Pe_{\text{ref}}} \nabla \cdot (D_i \nabla c_i) && (4.13)\\
\nabla \cdot (\epsilon \nabla \phi) &= -\rho_e - \rho_p && (4.14)\\
\rho_e &= \sum_i z_i c_i && (4.15)
\end{aligned}
$$

Finite element PNP model

We use a Galerkin finite element method to solve this PNP system. Among the advantages of this approach is that it lets us deal with complex geometry, with boundary conditions at material interfaces, and with sampled particle distributions in a very natural way.

Weak electrostatic equations

Let Ω be the entire computational domain and $\partial\Omega$ be its boundary. The outer subdomain region (I) will be called Ω_c, and the water-membrane interface will be Γ_I. The surface charge density at this interface is σ_p. The weak formulation of the Poisson equation is

$$\int_\Omega [\epsilon \nabla v \cdot \nabla \phi - v\rho_e + v\rho_p] + \int_{\Gamma_I} v\sigma_p - \int_{\partial\Omega} \epsilon v \nabla\phi \cdot \hat{\boldsymbol{n}} = 0 \quad \forall\, v \in H^1(\Omega)$$

where $H^1(\Omega)$ is the Sobolev space of all scalar-valued functions whose gradients are square integrable over Ω. The functions v are called "test functions." Note that the space H^1 includes functions with discontinuities in the normal components of their gradients, which is necessary because the normal component of the electric field will be discontinuous at dielectric interfaces. The boundary conditions for the Poisson equation are

- Specified potential drop between the inflow and outflow surfaces.
- The jump condition
$$\epsilon_1 \nabla\phi_1 \cdot \hat{\boldsymbol{n}} - \epsilon_2 \nabla\phi_2 \cdot \hat{\boldsymbol{n}} = \sigma_p$$
applies at the interface Γ_I. Note that this boundary condition is *automatically* satisfied by the solution to the weak equation above, and need not be included explicitly.
- $\nabla\phi \cdot \hat{\boldsymbol{n}} = 0$ on the radial boundaries of the computational domain.

Weak transport equations

For the cases studied in this work, only steady-state conditions with no bulk convective velocity are considered. Therefore, the first two terms on the left hand side of equation (4.13) are zero. Employing the Galerkin finite element method, this equation becomes, in weak form,

$$-\int_{\Omega_p} \boldsymbol{j}_i \cdot \nabla v_i + \int_{\partial\Omega_p} v_i \hat{\boldsymbol{n}} \cdot \boldsymbol{j}_i = 0 \quad \forall\, v_i \in H^1(\Omega_p)$$

where the particle flux $\boldsymbol{j}_i$ is

$$\boldsymbol{j}_i = -D_i z_i c_i \nabla\phi - \frac{D_i}{Pe_{\text{ref}}} \nabla c_i.$$

The boundary conditions for the transport equation are

- Zero normal flux on the pore surface and on the side walls of the computational domain.
- Specified concentrations at the inflow and outflow surfaces.
- Specified fluxes at the handshake surfaces.

Implementation

The model was implemented using the Sundance finite element toolkit, which allows rapid development of a high-performance simulator from a high-level "math-like" specification. Sundance is in turn built on the Trilinos family of solver components [38, 37, 26].

Particle-Based Model

There has been extensive research into ion transport in biological and synthetic nanopores using particle-based methods [52, 42, 17]. In general, the long time scales and large sizes of these systems makes overdampened Brownian dynamics (BD) the simulation method of choice, although attempts have also been made to use molecular dynamics (MD) simulations for short simulations of fairly small ion channels [47, 17, 20]. In general, particle based models permit inclusion of chemical effects, concentration effects and finite particle sizes, in exchange for substantially higher computational costs than continuum based models [7, 15]. For this reason, particle-based simulations are normally applied to fairly small simulation sytems where finite particle size and concentration effects over relatively short timescales are important. At the current time, all-atom MD simulations are generally restricted to less than 10^5 total particles and timescales well below one microsecond, while BD simulations can handle a similar or larger number of solute molecules (excluding water) and timescales that are orders of magnitude longer.

Formulation

Stochastic particle dynamics are based on the Langevin equation

$$m_i \frac{\mathrm{d}^2 \boldsymbol{x}_i(t)}{\mathrm{d}t^2} = \boldsymbol{F}_i(\boldsymbol{x}_i(t)) - m_i \gamma_i \frac{\mathrm{d}\boldsymbol{x}_i(t)}{\mathrm{d}t} + \boldsymbol{R}_i(t) \tag{4.16}$$

where i is a particle index ($i = 1, 2, ..., N$), m_i, and $\boldsymbol{x}_i$ are the mass and position, γ_i is the (possibly position-dependent) friction coefficient, $\boldsymbol{F}_i$ is the systematic force, and $\boldsymbol{R}_i(t)$ is the random force acting on the i-th particle at time t

Overdampened Brownian dynamics are a special case of the above equation in which the time step dt is sufficiently long that any particle momentum at time t is fully dissipated at time $t + \Delta t$ (equivalent to $\gamma \Delta t \gg 1$). In this case, the Langevin equation can be integrated using a simple explicit scheme [60]

$$\boldsymbol{x}_i(t + \Delta t) = \boldsymbol{x}_i(t) + \boldsymbol{F}_i(t) \frac{\Delta t}{\gamma_i m_i} + \boldsymbol{X}_i(\Delta t) \tag{4.17}$$

where $\boldsymbol{F}_i(t)$ is the systemic force acting on particle i at time t and $\boldsymbol{X}_i(\Delta t)$ is a Gaussian distributed noise with zero mean and standard deviation $2k_B T \Delta t (m_i \gamma_i)^{-1}$.

The systemic force contribution, $\boldsymbol{F}_i(t)$ consists of contributions from an applied electric field ($\boldsymbol{F}_{\text{field}}$), interactions with charges on the membrane wall ($\boldsymbol{F}_{\text{membrane}}$), and the reaction field interaction (steric and electrostatic) between this ion and all other ions in solution ($\boldsymbol{F}_{\text{reaction}}$):

$$\boldsymbol{F}_i(t) = \boldsymbol{F}_{i,\text{field}} + \boldsymbol{F}_{i,\text{membrane}} + \boldsymbol{F}_{i,\text{reaction}} \tag{4.18}$$

While $\boldsymbol{F}_{\text{field}}$ and $\boldsymbol{F}_{\text{pore}}$ can be pre-computed onto a grid and evaluated efficiently at each time step, the evaluation of the reaction field, $\boldsymbol{F}_{i,\text{reaction}} = \sum_i^{N-1} \sum_{j=i+1}^{N} F_{i,j,\text{electrostatic}} + F_{i,j,\text{steric}}$, is inherently an $O(N^2)$ calculation. Due to the non-uniform dielectric environment, commonly used accurate ways of accelerating long-range electrostatic calculations for multi-particle systems, such as Particle Mesh Ewald summation and Fast Multipole methods, are not appropriate for this system. While it should be possible to derive a way to accurately compensate for the presence of the membrane and pore in the long-range electrostatics, the development of such a model is outside the scope of this paper. Instead, we are applying switched electrostatics that smoothly scale electrostatic energies (and their first and second derivatives) to zero at the desired cutoff. When the shortest path between particles intersects the membrane, the electrostatic intereaction between the particles is computed along the shortest path through the solution and the steric interaction between the particles is omitted. This represents the exact solution for electrostatic forces in the presence of a perfect insulator, but is at best an approximate solution for membranes that are imperfect insulators. Earlier studies [24] have shown that the force lines do not penetrate the membrane when the ratio of channel diameter to membrane thickness is greater than $\sqrt{\frac{\epsilon_1}{2\epsilon_2} \ln \frac{\epsilon_1}{\epsilon_2}}$, or about 0.12 at $\epsilon_1 = 80$ and $\epsilon_2 = 2$, justifying the use of the shortest path approximation for the current simulation systems.

In reduced units, the modified electrostatic potential function Φ_{ij} for interaction between particles i and j with charges q_i and q_j is:

$$\Phi_{ij}(r) = \begin{cases} \frac{q_i q_j}{r} & \text{if } r < r_1 \\ q_i q_j \left(\frac{1}{r} - A(r-r_1)^3 - B(r-r_1)^4 - C\right) & \text{if } r_1 \leq r < r_c \\ 0 & \text{if } r_c \leq r \end{cases} \tag{4.19}$$

where the constants A, B, and C for the switcing function are

$$A = -\frac{5r_c - 2r_1}{r_c^3 (r_c - r_1)^2}$$
$$B = \frac{4r_c - 2r_1}{r_c^3 (r_c - r_1)^3}$$
$$C = \frac{1}{r_c} - \frac{A}{3}(r_c - r_1)^3 - \frac{B}{4}(r_c - r_1)^4$$

The choice of the cutoff length parameters r_1 and r_c represents a tradeoff between accuracy and performance. In the studies presented in this work, a range of cutoff parameters were tested; the results presented in the following sections were run with cutoffs sufficiently large to achieve complete interactions between all ions in the particle system.

Implementation

The simulation domain for the particle model is a three-dimensional model of an axisymmetric cylinder of length l_c and radius r_c centered on the coordinate origin and aligned with the z-axis. The cylinder is capped at each end by a hemisphere of radius r_h. The medium inside the cylinder and the hemispherical domains is assumed to be an aqueous medium with dielectric $\epsilon = 80$; the volume between $z = -l_c/2$ and $z = l_c/2$ that does not fall inside the cylinder is assumed to be an insulator with dielectric $\epsilon = 1$. Other volume outside the hemispheres is assumed to be handled externally (e.g. by the continuum simulation environment), but this system could also be modified as a simple reaction field if desired.

The hemispheres at the two ends of the cylinder are arbitrarily labeled "inlet" and "outlet." Each hemisphere has radius r_t which is divided into two regions, an inner region of radius r_i and an outer handshake shell of radius $r_h = r_t - r_i$. Each region is individually concentration controlled such that the average concentrations of ionic species in the hemisphere and the associated half of the channel is maintained at the desired levels. When a charged particle crosses the midplane boundary perpendicular to the center of the channel, a particle is randomly chosen from one handshake region and placed in the other handshake region to maintain the desired concentration gradient across the simulation system.

Chemical and electrostatic effects of the surface of the membrane are handled explicitly using an atomic representation of the membrane. Since the pore geometry is not varied during the course of the BD simulation, electrostatic and steric effects are precomputed onto a structured grid. Forces acting on particles in solution are computed from the grid using Hermite interpolation. In the case of an axisymmetric simulation system, this interpolation can be performed on a two-dimensional grid. To improve the stability of the simulation at long integration timesteps, solution ions that come within van der Waals contact with the membrane surface are reflected outward from the wall before their steric interactions are computed. This results in capping of steric interactions in the immediate contact layer at the membrane, which in turn reduces the incidence of particles being ejected from the walls due to the sharp (twelfth-power) repulsive Lennard-Jones potential. Charges are distributed uniformly on all membrane atoms falling within 0.25 nm of the channel wall, and are scaled to obtain the desired charge per unit area.

Electromotive force due to applied electric potentials is supported only in the multiscale atomistic-to-continuum multiscale simulations. The details of this implementation are described in the section on multiscale coupling.

Multiscale Coupling

Introduction

The term multiscale simulations is commonly used to describe model systems whose characteristic scales (typically spatial or temporal) permit the system simulation to be divided into two or more separate simulation models linked through a shared boundary. Multiscale simulations are finding increasing use for modeling systems where the actions of small-scale, tight-binding events have looser coupling to the larger-scale system evolution. Multiscale multiphysics simulations (sometimes referred to as "hybrid methods") apply disparate physics models for fine-grained and coarse-grained regions of the multiscale simulation. Since these types of simulations are the focus of this report, we will from here on use the term "multiscale" to mean "multiscale multiphysics."

Multiscale simulations can be coarsely divided into two main categories. In concerted multiscale simulations, the differently represented sections of the simulation system are evolved together, with information transfer performed between the models at every step. In stepwise multiscale simulations, the models progress independently, and the simulation results from each stage are used as initial parameters or boundary conditions for subsequent stages. Each of these approaches is appropriate for different simulation types; concerted multiscale simulations permit very tight integration of coarse-grained models into fine-grained simulations while stepwise multiscale simulations are better suited for providing fine-grained foundations for long-timescale coarse-grained simulations.

Multiscale simulations have gained significant traction in select simulation fields such as coupled quantum-mechanical/molecular mechanics (QM/MM) systems [62]. Domain decomposition for multiscale simulations of fluidic systems was explored by Hadjiconstantinou [25], who showed that high efficiencies can be achieved when a multiscale system is appropriate for the Schwarz alternating method [53], in which the problem is divided into subdomains that are solved in an alternating fashion until convergence is reached. Later research applied similar methods to various microfluidic and nanofluidic simulation systems [4, 50]. For a thorough review of multiscale phenomena in micro- and nanofluidics, the reader is directed to a recent review by Hu and Li [29].

In the current work, for the simulation of steady state ionic fluxes, a multiscale coupling method was developed based on the Schwarz alternating method. The sections below highlight the main aspects of this method; more details can be found in our paper on this topic [2].

Multiscale formulation

As detailed in the previous sections, a BD particle model is used to achieve a good physical representation in the confined geometry of the nanopore, while a computationally less de-

manding continuum PNP model is used to resolve phenomena in the far-field, away from the nanopore, as illustrated in Figure 4.1. Since the phenomena in those areas are coupled, it is necessary to exchange information between the two models in order to obtain a consistent solution throughout the domain.

More specifically, on the particle side, information is needed to compute all contributions to the forces in equation (4.18). While this force computation is straightforward in a pure atomistic system, the solution here is complicated by the fact that the force contributions are strongly coupled between the atomistic and continuum regions. This is especially true for the electrostatic interactions, which are very long-range. For a sufficiently small number of particles, the force contribution could be obtained by solving all electrostatic interactions at the continuum level, with explicit charges placed at the particle positions in the atomic simulation. This becomes computationally intractable however, for large numbers of particles or for long simulation durations. Therefore, in order to make the force computation in the particle domain tractable, some core assumptions are made regarding the treatment of the electrostatic interactions:

- The electric field resulting from the applied (driving) electric potential is computed from an all-continuum solution over the full simulation domain, permitting $F_{i,field}$ to be obtained through $O(N)$ evaluations at the continuum level.
- The contributions of membrane charges on the area of the membrane outside of the BD domain as well as the contributions of bulk charges in the continuum fluid zone are similarly taken into account on the continuum level.
- Membrane charges within the atomistic domain are assumed to be invariant. This permits $F_{i,membrane}$ to be pre-computed onto a grid using direct summation on the BD level and then evaluated throughout the domain with Hermite interpolations.
- The contributions from ions in the fluid in the BD domain are taken into account through direct summation of the Coulomb interactions on the BD level, as discussed in the particle model section.

The other piece of information that is needed on the particle level is the concentration of the ionic species at the interface between the continuum and the particle domain, to be used as concentration boundary conditions at those locations for the particle model. At each interface, the averages of the concentrations over that interface, as obtained from the continuum model, were used as the corresponding values for the particle level boundary conditions.

On the continuum level, values for the species flux boundary conditions are provided by the flux values extracted from the particle simulations (averaged over all replica simulations). The electric potential is computed by the continuum solver over the full domain (far-field fluid, membrane, and pore area), and takes into account the contributions of the externally applied field, the membrane charges, and the bulk charge density. In the current work, the contribution of both the membrane charges and the bulk charges that are located inside the

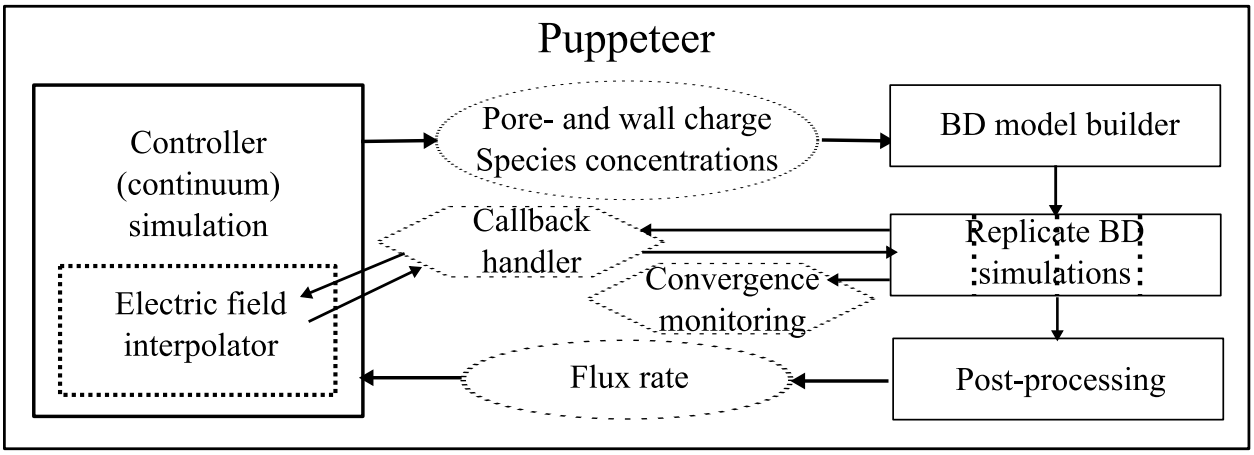

Figure 4.2. Flow chart for multiscale electrodesalination simulations.

particle domain are neglected on the continuum level. As long as the particle domain extends far enough away from the pore entrance and exit, this is assumed to be a minor approximation on the continuum level as the ions in the bulk of the pore shield the membrane wall charges inside the pore. Note that on the particle level, those contributions are properly taken into account through direct summation of Coulomb interactions over the charges involved.

We are investigating making the bulk charge density inside the particle domain available to the continuum solver by sampling the particle fields. This could result in significant performance gains on the particle level as it would make it possible to account for long range interactions on the continuum level. The noise in sampled particle fields is a concern for the continuum solver, however. Proper smoothing of the sampled fields is the topic of ongoing research.

Timescales between the continuum and atomistic models have notable overlap, but the overall time evolution of the system is still far too great to track the entire simulation using BD methods. In a fully time integrated scheme, this could be accommodated through projective integration [54]. In the current study the focus was on steady-state transport through the nanopore. Therefore, the continuum and particle simulations were run alternatingly, until they converged to a steady state solution.

Implementation

The sequence of the multiscale algorithm and the flow of information between the continuum and particle components is summarized in Figure 4.2. Note that this simulation approach deviates from a traditional Schwarz-decomposition scheme due to the field evaluation callbacks between the BD and continuum components. The "puppeteer" component sets up the

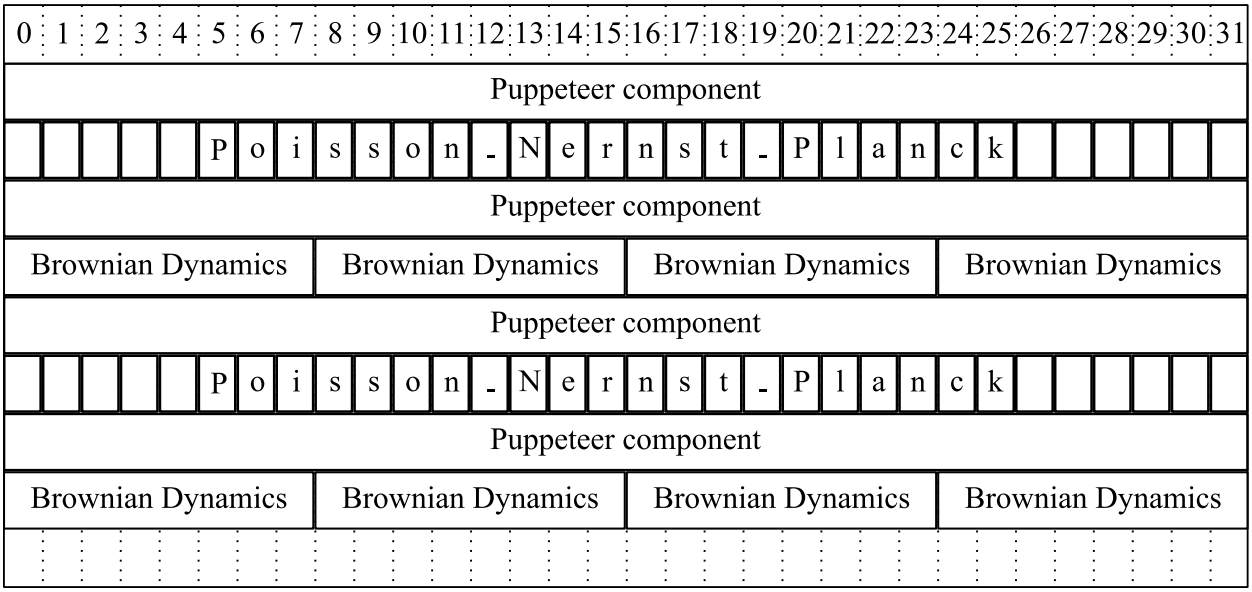

Figure 4.3. Schematic management of a multiscale simulation on 32 nodes with MPI-unaware continuum simulations and four replicate BD simulations. The rows in this table represent successive steps in the program execution. The colums represent the nodes on which the steps are executed.

problem and contains all higher-level logic to coordinate the simulation iterations.

Independent components for the continuum and particle simulations were written as C++ libraries, while the higher-level logic puppeteer was written in Python. Using SWIG [1], the C++ components were made available to Python, and vice versa. More details on this implementation can be found in [2].

Note that since destructive updates to the continuum simulation are not permitted during the BD simulations, callbacks from the BD simulation to the continuum component can be performed in parallel environments where the communication group size for the BD simulation differs from that of the continuum simulation. A conceptual schematic of this is shown in Figure 4.3. In this specific example, the BD simulation relied on 4 replica simulations, each running on 8 nodes with MPI. As the continuum simulation is very fast compared to the particle simulations (minutes vs. hours), the continuum simulations were run in serial, with identical continuum components assigned to all processors. The added cost in replicating continuum data between nodes is negligible (at most a few megabytes) and eliminates any MPI communication associated with the 10^6 evaluations of external field effects on the BD particles.

As is indicated in Figure 4.2, the high-level (Python) puppeteer component mediates both the transfer of boundary conditions and field-evaluation callbacks between the continuum and

BD components. The performance cost associated with transferring boundary conditions is near-zero (sub-milliseconds for multiple hours of BD simulations), and the total cost imposed for field evaluation callbacks is close to 1% of total simulation time. For this reason, we feel that the improved flexibility and loose coupling obtained by routing the field callbacks through the high-level puppeteer component is well justified.

Chapter 5

Results and Discussion

Membrane Characterization

Track-Etched Membrane Contact Angle Measurements

Although we initially modified the track-etched membranes using oxygen plasma with some success, we focused our efforts on UV-ozone followed by thermal grafting for two reasons: 1) it provides an avenue to fix charges of either polarity, and 2) this technique provides a more permanent surface modification compared to either oxygen plasma, or UV-ozone treatment itself. Using SEM micrographs we determined that membranes exposed to UV-ozone longer than 60 minutes were irreversibly damaged as shown in Figure 5.1. As a result, we studied UV-exposure times necessary to successfully graft the monomers with minimal surface damage and found that 15 minute UV-exposures were sufficient for surface activation and caused no visible damage to the surface or pores. In addition, we found that as the monomer concentration was increased, the likelihood of the grafted material to plug the pores was more prevalent. For this reason we concentrated on using monomer concentrations ranging between 0.1 – 1.0 wt% and 5 minute grafting. A SEM micrograph of an (1.0 wt% : 5 minute) AAc grafted membrane is shown in Figure 5.2. The modified membranes' wetting properties were characterized using contact angle measurements. Figure 5.3 compares the contact angle measurements for modified membranes stored in ambient conditions after two weeks verses a native polycarbonate track etched membrane. The contact angles decreased between (5 – 20°) versus the unmodified polycarbonate track etch membrane depending on the grafted monomer.

Track-Etched Membrane Surface Characterization

The surface functional groups grafted onto the track-etched membranes were not detectable by X-ray photoelectron spectroscopy or by FTIR. Therefore, surface morphology was examined using high resolution FESEM. Shown in Figure 5.4 are the surface features of an untreated track-etched membrane. Both pores and surface cracks (from the etching process) are visible. Figure 5.5 shows a series of micrographs for membranes that have been grafted with monomers on one surface as described above. (a) and (b) correspond to the front and

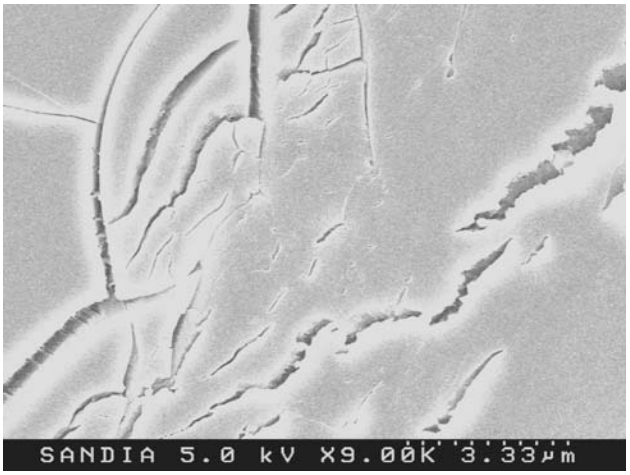

Figure 5.1. SEM micrograph of a PCTE membrane damaged by a 60 minute UV-ozone exposure.

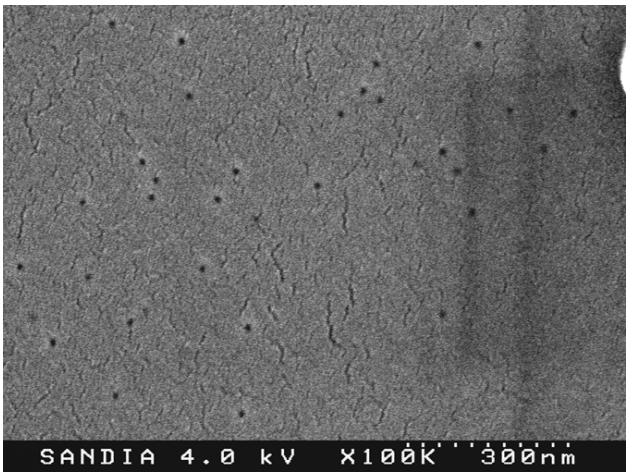

Figure 5.2. SEM micrograph of a PCTE membrane exposed to UV-ozone for 15 minutes, with subsequent 5 minute thermal graft of 1.0 wt % AAc.

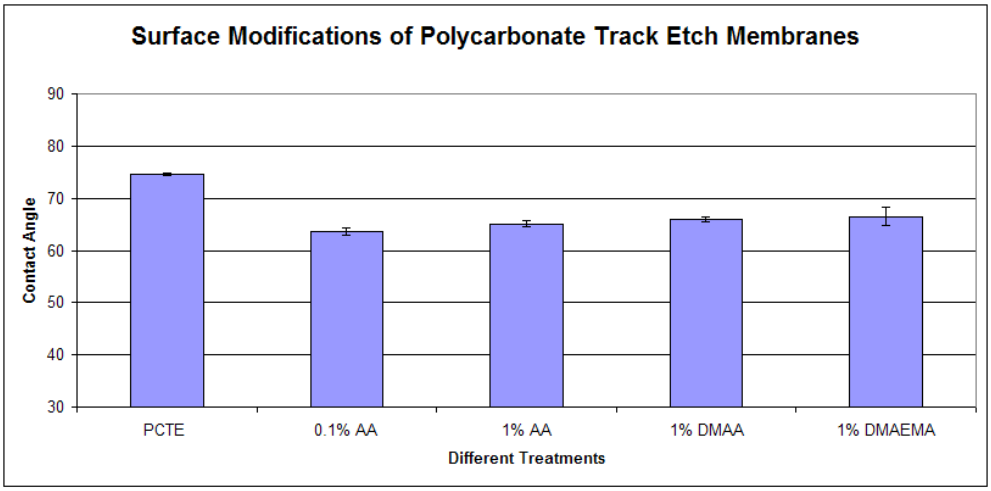

Figure 5.3. Contact angle comparison of thermally grafted monomers verses an un-modified PCTE membrane. The data represents contact angles taken for two week old membranes.

back sides of a membrane grafted in 1 wt % acrylic acid solution. (c) and (d) correspond to the front and back sides of a membrane that was grafted in 1 % dimethylacrylamide solutions. (e) and (f) are the front and back sides of a membrane that was grafted in 1 % Dimethylaminoethyl methacrylate solution. For the grafted sides of the membranes in (a), (c), and (e) no pores or only very light dimples are observed indicating that the pores are partially or completely covered by the grafting monomer. In (b), (d), and (f), clear pores are still observed. A schematic of what the pores may look like when grafted in 1 wt % monomer solutions is shown in Figure 5.6. It is unknown at this point how thick the grafted layers are, their graft density (chains/nm^2), or how deeply the grafted polymers may penetrate into the pores.

Track-Etched Membrane Surface Charge

The surface charge of each of the membrane samples was measured using the streaming current technique. As shown in Figure 5.7, the ungrafted PCTE membranes had a more positive surface charge than all of the grafted membranes. Membranes grafted with acrylic acid had the most negative surface charge at high pH. This result is reasonable given that the acrylic acid grafts introduce weak carboxylic acid groups to the membrane surface. Under high pH conditions, the carboxylic acids become deprotonated and a negative surface charge results. The sample grafted with 1 wt % monomer solution had a more negative zeta potential than the 0.1 wt % monomer solution indicating that more surface charges were present and that most likely a higher grafting density was obtained with the 1 wt % solution. The DMAA and DMAEMA grafts also moved the zeta potential to more negative

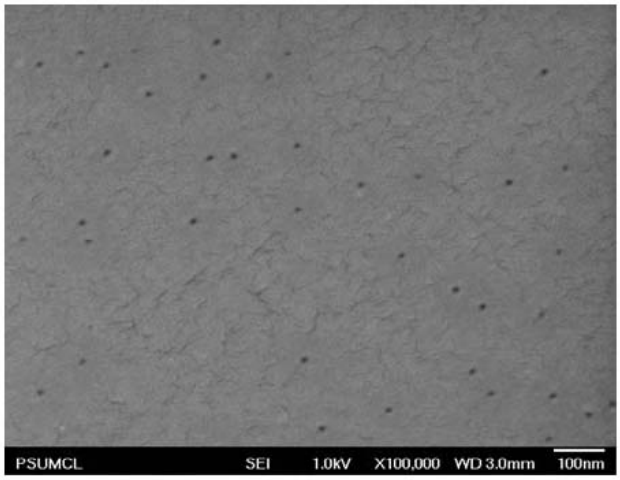

Figure 5.4. Surface features of an unmodified PCTE membrane.

values compared to the ungrafted PCTE membrane, but to a lesser extent than with the charged, acrylic acid grafts. The DMAA and DMAEMA grafts introduce polar species onto the membrane surface which may increase their adsorption capacity for negatively charged ions from solution, thus pushing the zeta potential more negative.

Membrane Transport Properties

Measurements

Polyaniline Membrane Transport

Doped and dedoped PANI membranes were characterized for their pore structure and transport properties. Small angle neutron scattering (SANS) was performed on PANI membranes doped with camphorsulfonic acid at a 3:1 molar ratio. SANS measurements were conducted on both as cast and dedoped PANI membranes filled with D_2O. The neutron scattering intensities as a function of scattering vector are shown in Figure 5.8. Scattering features are observed for both curves at scattering vectors around 0.1 $Å^{-1}$ which indicates that similar size features are present in both samples. A small scattering length density contrast existed in the doped membranes between camphorsulfonic acid and PANI, probably as a result of the proton density in each species. When the membrane was dedoped, the scattering intensity increased greatly indicating that D_2O-filled pores were created.

Glucose permeability was used as a probe of the membrane transport properties as a

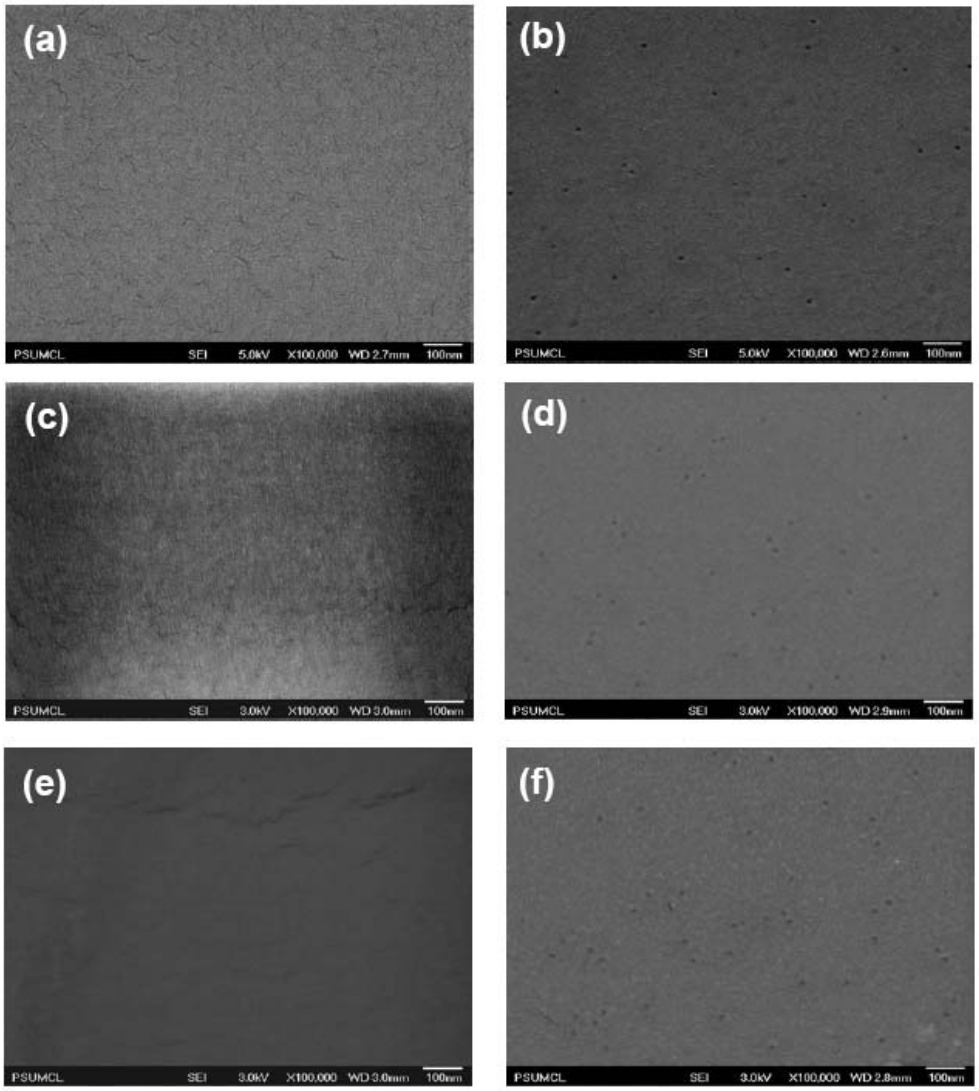

Figure 5.5. Front and back comparison of membranes grafted with various monomers: (a) and (b) correspond to the front and back sides of a membrane grafted in 1 wt % acrylic acid solution. (c) and (d) correspond to the front and back sides of a membrane that was grafted in 1 % dimethylacrylamide solutions. (e) and (f) are the front and back sides of a membrane that was grafted in 1 % Dimethylaminoethyl methacrylate solution.

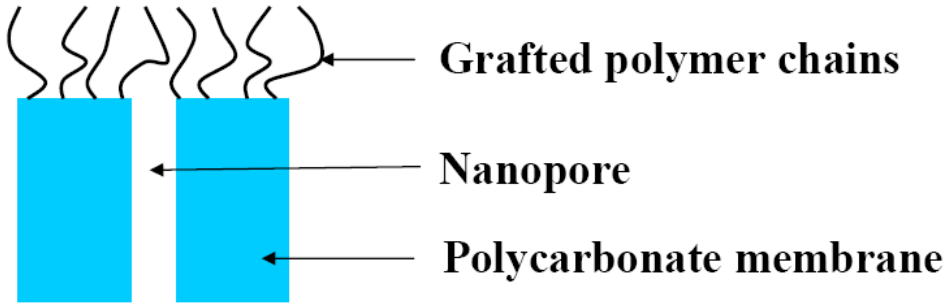

Figure 5.6. Schematic of pore cross section showing grafted membrane surface.

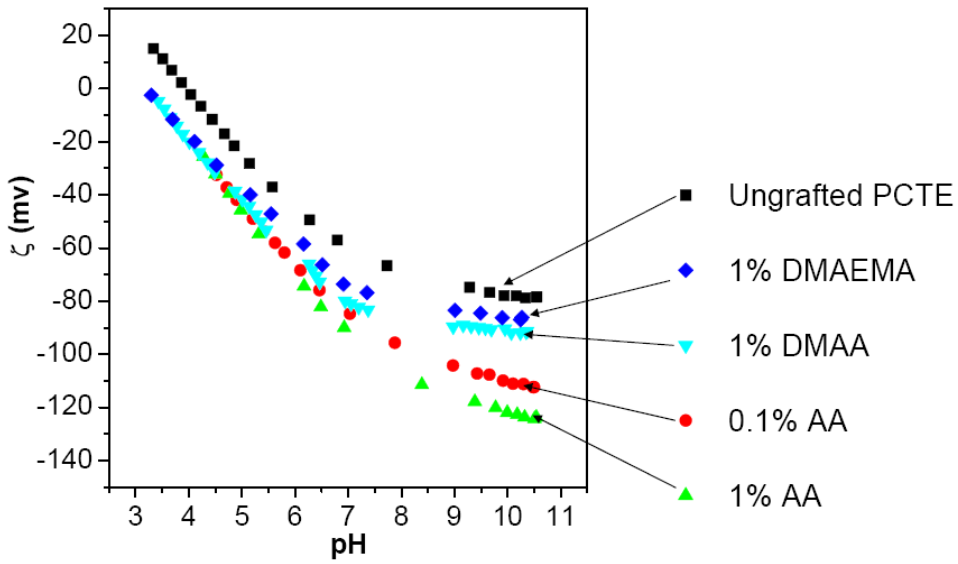

Figure 5.7. Computed zeta potential of modified PCTE membranes as a function of pH.

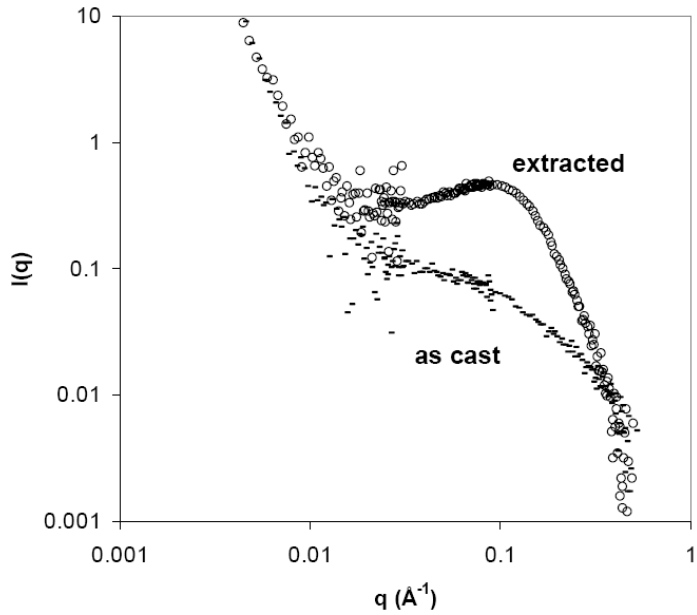

Figure 5.8. Small-angle neutron scattering curves for as cast and undoped membranes immersed in D2O.

function of doping ratio. Shown in Figure 5.9 is the glucose permeability of thin-film composite membranes as a function of doping ratio - after the membranes were dedoped. The thickness of the membranes in this study was kept constant by controlling the PANI concentration and spin speed. This permeability data demonstrates that the porosity and thus the transport properties of molecularly doped PANI membranes can be controlled using this approach. Further studies will focus on the size and doping ratio effect for other strong acid dopants. Additionally, other types of permeant molecules and ions will be investigated.

Track-Etched Membrane Transport Properties

The sodium chloride permeability and field-driven transport resistance for the track-etched membranes is shown in Figure 5.10a. Both of these transport measurements tend to track with one another. This correlation is interesting given that the permeability is a concentration gradient-driven phenomenon and the resistance was determined using a field-driven measurement. Interestingly, the acrylic acid grafts that introduced negative charges on the surface, had the lowest permeability and highest resistance values. It appears as though the negative surface charges decreased transport by screening charges from entering the pores. The case of the uncharged grafts is not so clear. There could be two mechanisms to consider. Both the DMAA and DMAEMA grafts were shown to partially or completely cover the pores which would impede transport. However, contact angle measurements show that both of these grafts increase the hydrophilicity of the membrane which could in turn increase the

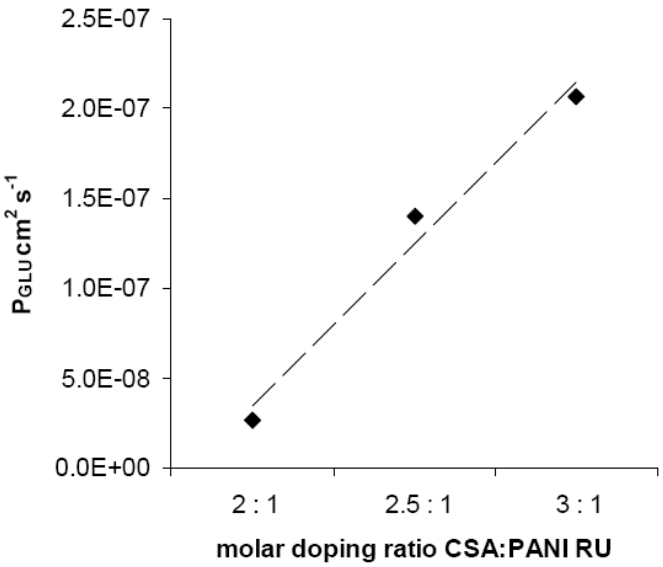

Figure 5.9. Glucose diffusion as a function of doping ratio in PANI membranes.

transport through the nanopores. Figure 5.10b shows the correlation between surface charge and sodium chloride permeability. The results are consistent between surface charge density, monomer grafting concentration, and transport properties for the acrylic acid grafts. The picture is not so clear for the DMAA and DMAEMA grafts. DMAA has higher resistance and lower permeability than the ungrafted PCTE sample, which could be expected from the pore blockage effect. DMAEMA has a much higher permeability than the ungrafted sample, but a higher resistance as well. Therefore in concentration-gradient driven measurements, the passage of sodium chloride is relatively facile as compared to the ungrafted sample, but there is more resistance to transport in the field-driven experiments. A possible explanation for this difference between DMAA and DMAEMA grafts is that the DMAEMA grafts are longer and may respond to the potential applied to the membrane during field-driven experiments. These effects between surface charge and transport properties warrant further investigation.

Simulations

The multiscale coupling scheme outlined above has been applied to the simulation of ionic fluxes through a nanopore, with a diameter of 5 nm and a length of 50 nm (Figure 5.11). In the simulations, the three-dimensional Brownian Dynamics (BD) domain covered the full nanopore as well as two hemispheric regions with a 10 nm radius at the entrance and the exit

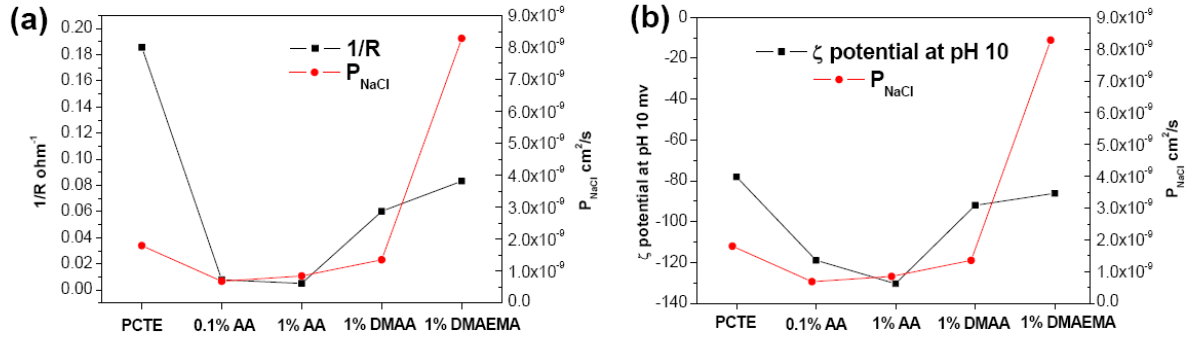

Figure 5.10. Comparison of modified PCTE membranes showing relationship of potential-driven and diffusive fluxes to zeta potential.

of the pore. The continuum species transport equations were solved on a 2D axisymmetric domain extending from the edge of the BD domain up to 50 nm away from the pore in the streamwise direction, and 25 nm in the radial direction, both upstream and downstream from the pore. The Poisson equation for the electric potential was solved on a 2D axisymmetric domain, 150 nm long and 25 nm in the radial direction, containing an axial slice of the pore, the membrane as well as the continuum species transport zones upstream and downstream from the pore. In the fluid, the relative dielectric permittivity was set to 78, while in the membrane, it was set to 2.

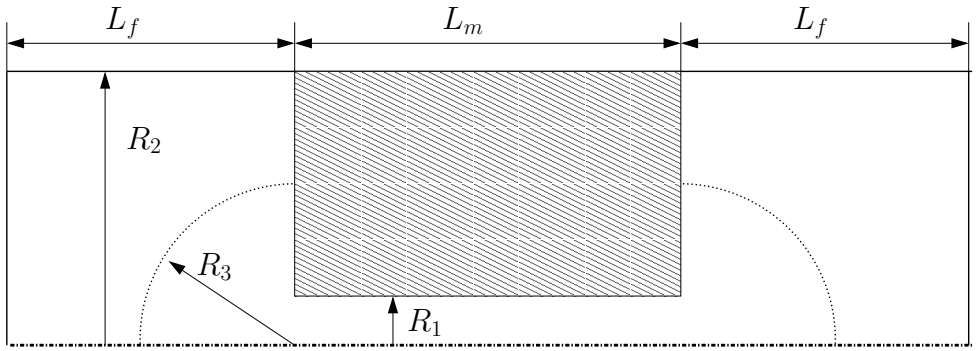

Figure 5.11. Computational domain

Starting from an analytical guess for the species fluxes, the simulations iterate between the continuum and the BD modules until the species flux through the nanopore converges to a steady value. For the computation of the ionic fluxes through the nanopore region with BD, 10 replica simulations were used, which were run for 10 μs each. As Figure 5.12

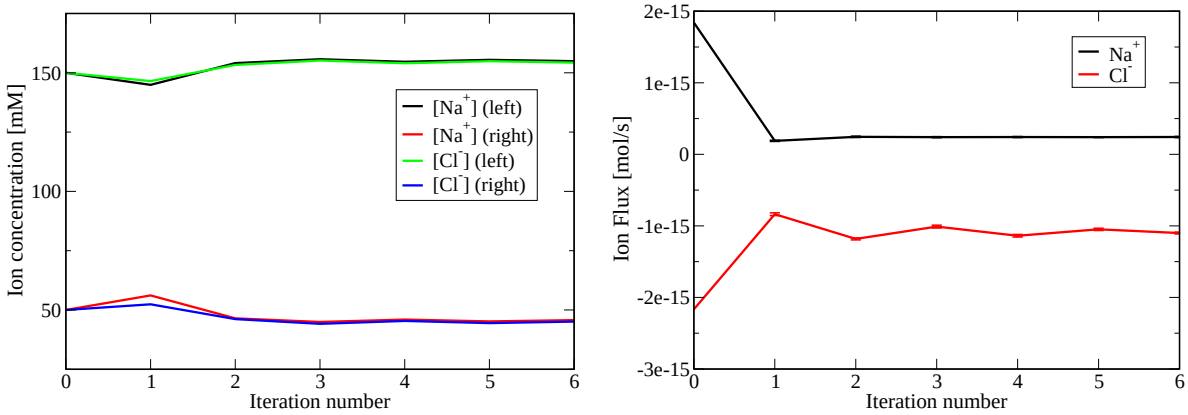

(a) Ion concentrations at the left and right continuum/pore interface

(b) Ion fluxes through the pore, with their standard deviation over 10 replicas indicated with error bars

Figure 5.12. Convergence of ion concentrations and fluxes with PNP/BD iteration count for a case with an applied potential of 0.2 V, c_1 = 150 mM, c_2 = 050 mM, and a wall charge inside the pore of +0.1 C/m^2

illustrates, after 2–3 iterations, the changes in the flux values between successive iterations were generally of the same order as the standard deviation of the fluxes across those 10 replicas.

Figure 5.13 shows the steady state concentration fields for the sodium and chloride ions for the case with a 150 mM NaCl concentration at the domain inlet and 50 mM at the outlet. A 200 mV potential difference was applied across the membrane. The pore surface inside the membrane had a surface charge of -0.01 C/m^2. The values of the concentration fields in the continuum zone were extracted directly from the Sundance solver. To get the concentration fields inside the nanopore, sampled particle fields from the BD solver were binned and projected onto a mesh on the continuum level. Despite the noise in the sampled concentration fields, it is clear that the concentration fields match up well at the interfaces between the continuum and particle models. As can be expected, the bulk of the concentration drop occurs across the nanopore region, with only about 1 mM concentration drop across the continuum entrance and exit regions.

Given the negative charge on the pore surface inside the membrane, the positive ions preferentially migrate towards the pore surface to shield the negative wall charge. As a result, the sodium ion concentration shows a maximum near the pore wall and the chloride ion concentration a minimum. The net result is a positive bulk charge in the fluid near the pore wall, as indicated by Figure 5.14, which shows the sum of the concentration fields in Figure 5.13. The predicted ionic fluxes through the pore for this case were $8.0 \pm 0.1 \times 10^{-16}$mol/s for the sodium ion and $-5.7 \pm 1.6 \times 10^{-17}$mol/s for the chloride ion (where a negative flux indicates an upstream flux from right to left).

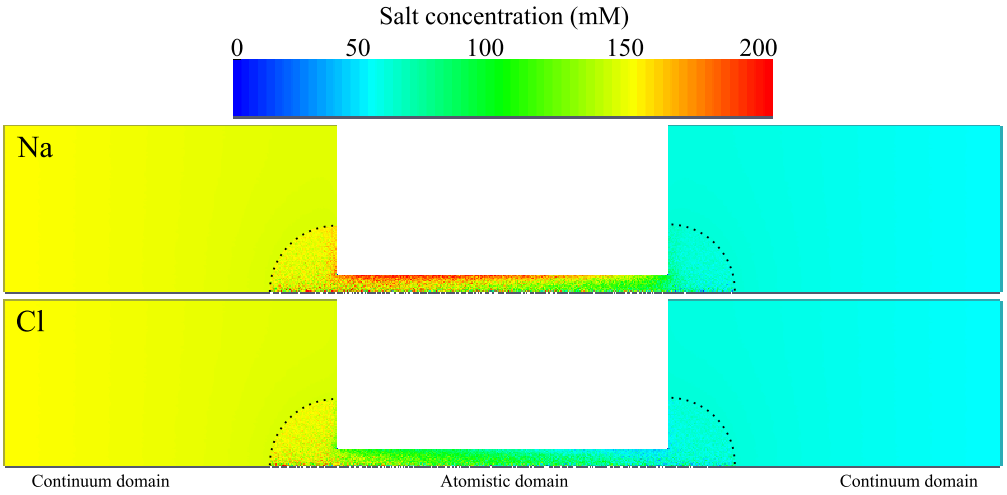

Figure 5.13. Sodium (top) and chloride (bottom) concentration fields in electrodialysis through a negatively charged pore through a membrane. An axial cross section of the pore is shown in the center, in between a continuum species transport zone upstream and downstream. The membrane material surrounding the pore is not shown. Black dotted lines indicate the location of the handshake region between the continuum and BD models.

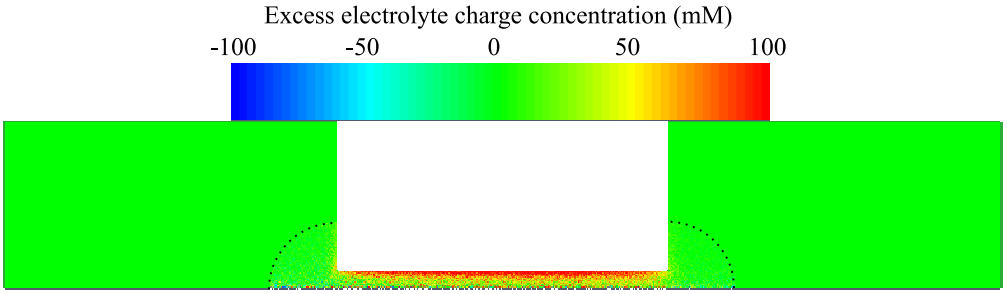

Figure 5.14. Solution charge density (represented as signed electrolyte concentration) in electrodialysis through a negatively charged nanoporous desalination membrane.

The particle representation inside the nanopore is essential in these simulations, as the continuum PNP formulation ignores particle diameters, and would therefore pack too many ions too close to the surface in order to shield the negative wall charge. The continuum formulation, on the other hand, is well suited to compute the effect of the externally applied potential difference across the membrane, taking into account the different dielectric permittivities between the membrane and the fluid. The two formulations therefore complement each other well.

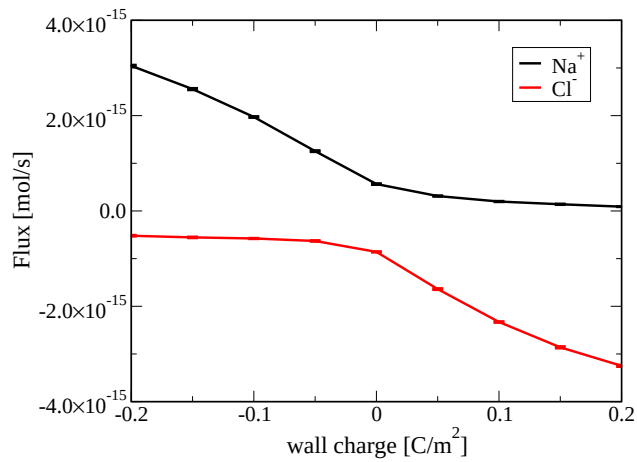

Figure 5.15. Fluxes for 0.2V, c_1 = 150 mM, c_2 = 150 mM

The multiscale simulation system described above has further been applied to a parametric study of the effects of membrane surface charge on electrodialysis in nanopores. These studies demonstrate that, at physically relevant NaCl concentrations and electric field gradients, a nanopore with 5 nm diameter can be made completely anion or cation selective by introducing a pore charge of modest magnitude and an opposite sign. Figure 5.15 demonstrates the dependence of field-driven transport through the nanopore with identical salt concentration on both sides of the pore (150 mM) with a 0.2 V electric potential applied across the simulation system. From these results, it is evident that the gating effect is relatively symmetrical, with the differences in Na and Cl fluxes through an uncharged pore being proportional to their diffusivity coefficients. The results at the highest pore charges (-0.2 C/m^2 and 0.2 C/m^2) are somewhat less reliable than the lower pore potentials due to limitations with the way ion concentrations at the boundaries between the continuum and atomistic regions are handled, but these parametric studies show complete gating well before these higher potentials.

The gating effect created by the pore charge can overcome concentration gradients across the nanoporous membranes, as illustrated in Figure 5.16. These conditions are particularly important for the operation of electrodialysis membranes, since the diluate stream will by design always have a lower salt concentration than the concentrate stream (see Figure 1.1). In a coflow electrodialysis system, this salt gradient will increase along the length of the

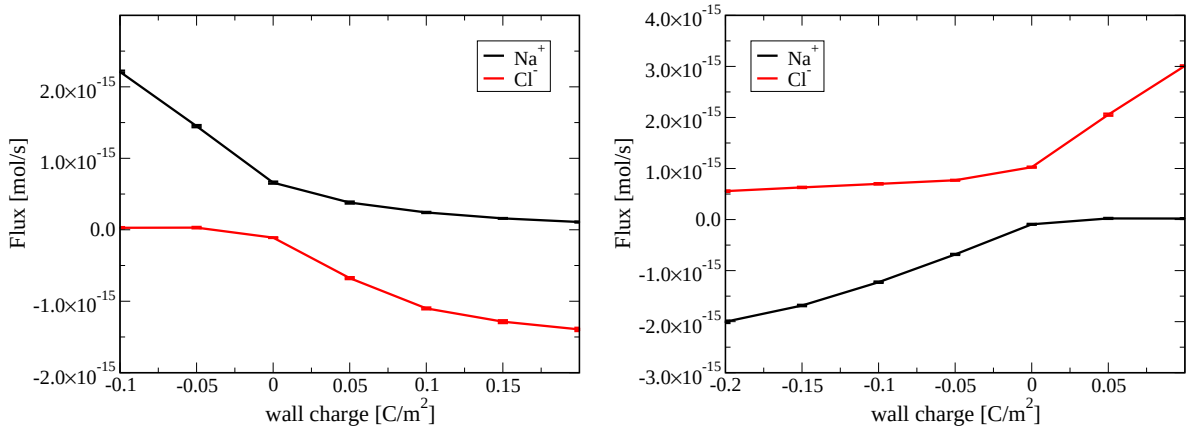

(a) Applied potential = 0.2V (b) Applied potential = -0.2V

Figure 5.16. Fluxes for c_1 = 150 mM, c_2 = 050 mM

membrane, whereas a counterflow system will have constant concentration gradient across the membrane. The simulation systems in Figure 5.16 are identical except for the direction of the applied electric potential, showing that a combination of the electric potential and pore charge can be used to exclude a given ionic species and to force a desired species against a reasonable concentration gradient. Efforts are ongoing to assess the effects of higher pore charges and electric potentials on the exclusion or forced transport of ionic species through the pores.

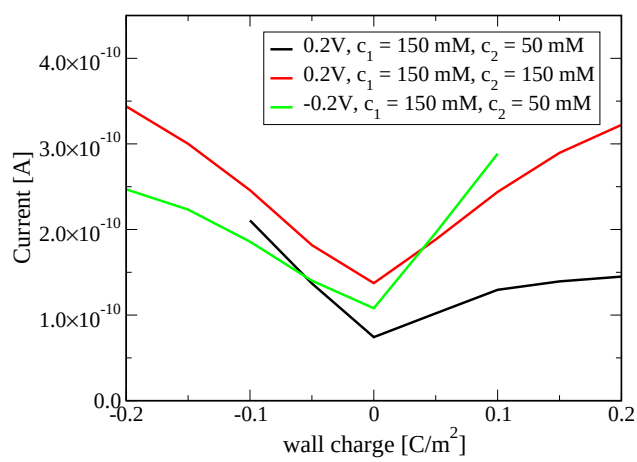

Figure 5.17. Total currents as a function of wall charge inside pore.

The total currents from the parameteric studies above are illustrated in Figure 5.17. Like the preceding results, these show that all the systems experience accelerated transport of the

non-blocked species through the membrane as the pore potential is increased. This effect is presumably due to the increased effective ion concentration inside the pore, which is required to counteract the electric charge on the pore wall. Further studies are planned to better identify the limits of this effect and to identify possible non-physical solute behavior at very high pore charges. These observation stand in contrast to the experimental measurements in this study, in which the membranes with highest ζ-potential were observed to have lower ionic fluxes than less charged membranes. Further studies, both experimental and computational, will be needed to quantify the influence of finite reservoir volumes in the experimental measurements and to better establish the relation between the ζ-potential measured at the membrane surfaces and the potential conditions existing inside the nanopores.

The detailed concentration profiles obtained for the system in Figure 5.16(a) are illustrated in the following figures. This shows clearly that as the wall potential inside the pore is varied, the concentration profiles of Na (Figure 5.18) and Cl (Figure 5.19) respond strongly, resulting in significant gating effects at pore potentials of ± 0.05 C/m^2 and near-complete exclusion of an ionic species at ± 0.1 C/m^2.

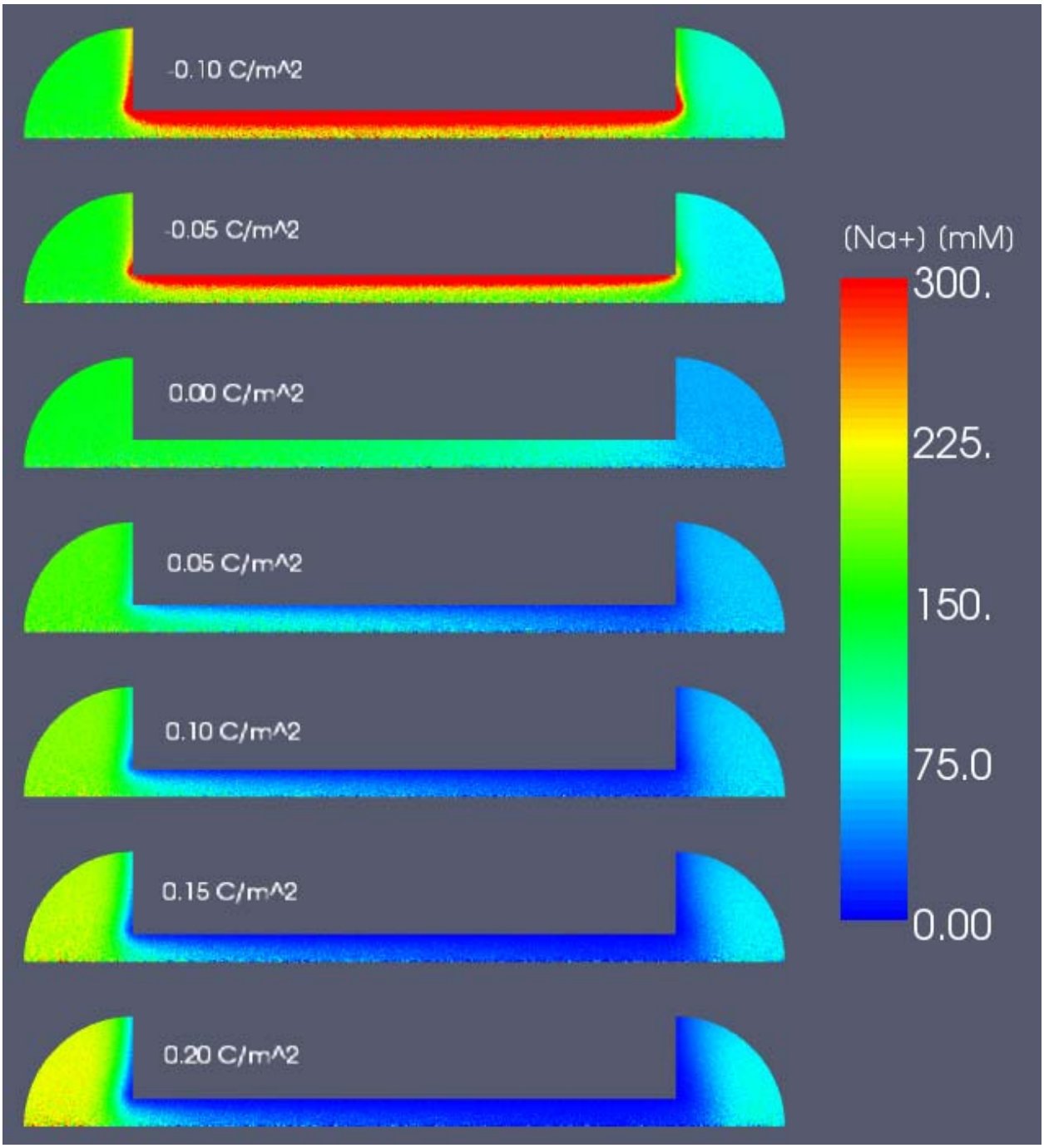

Figure 5.18. [Na^+] from sampled BD fields for case of 0.2V, c_1 = 150 mM, c_2 = 050 mM as a function of the wall charge inside the pore. The wall charge was varied from -0.1 C/m^2 (top panel) to 0.2 C/m^2 (bottom panel) in 0.05 C/m^2 increments.

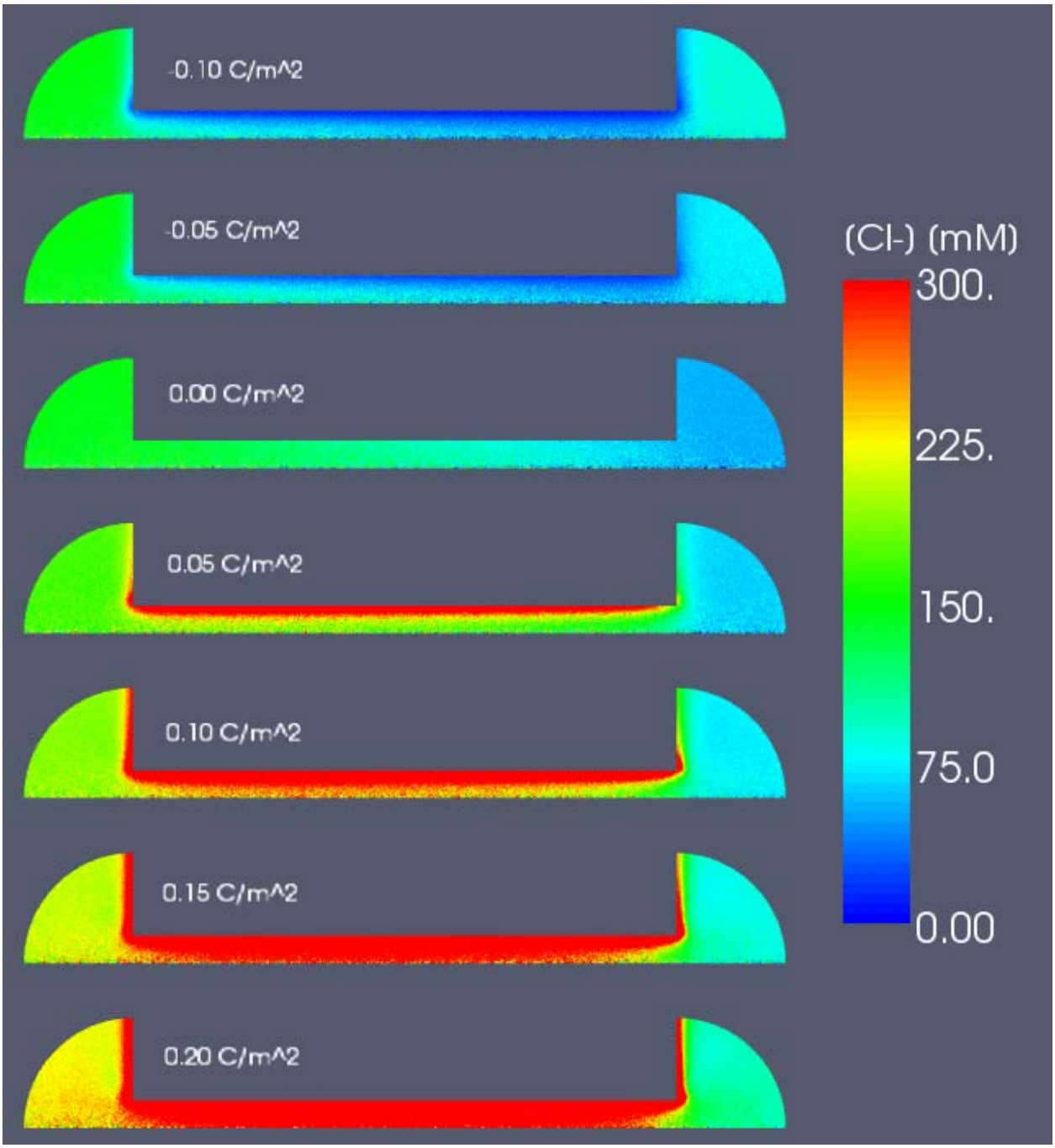

Figure 5.19. [Cl^-] from sampled BD fields for case of 0.2V, c_1 = 150 mM, c_2 = 050 mM as a function of the wall charge inside the pore. The wall charge was varied from -0.1 C/m^2 (top panel) to 0.2 C/m^2 (bottom panel) in 0.05 C/m^2 increments.

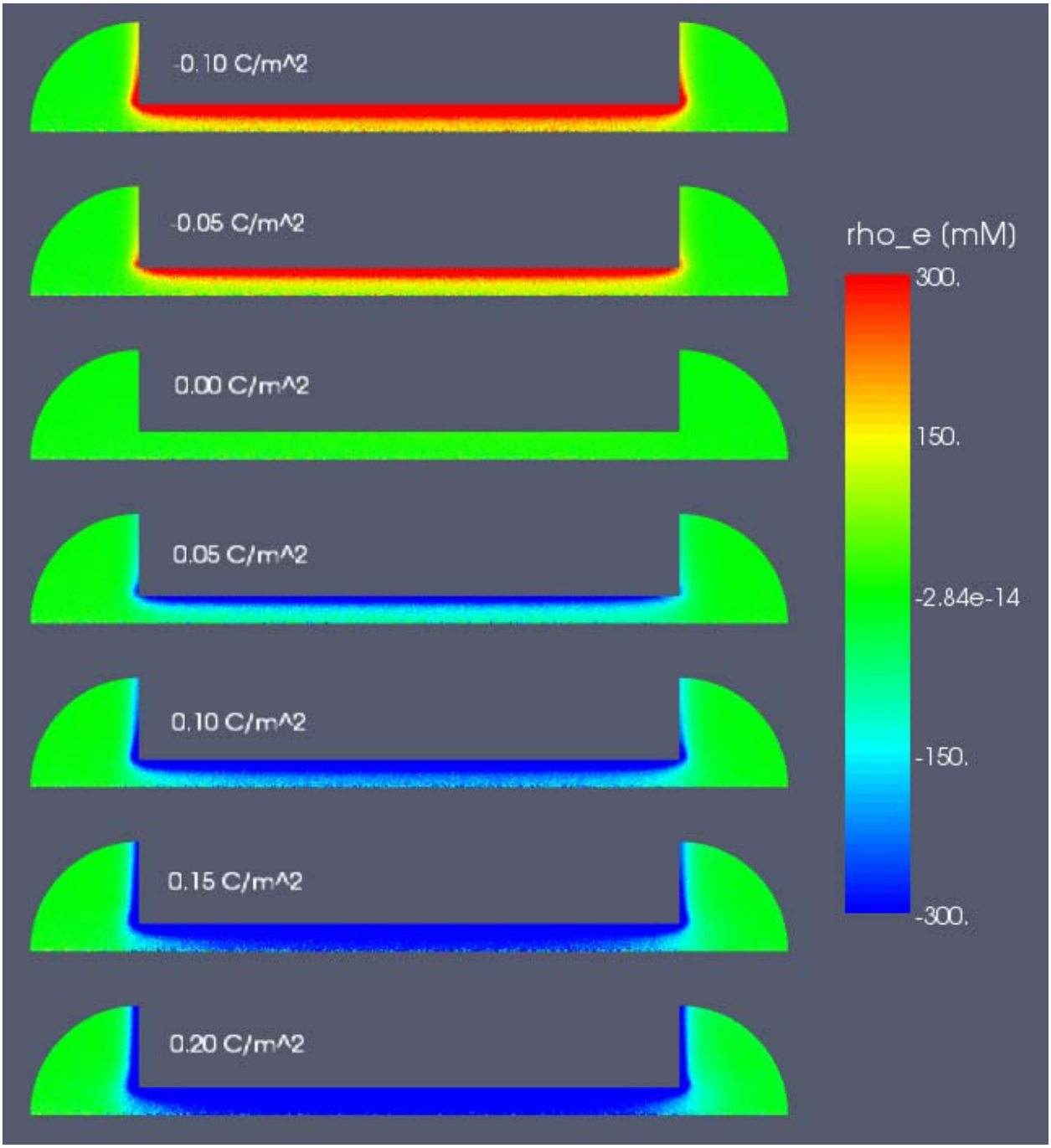

Figure 5.20. Bulk charge concentration from sampled BD fields for case of 0.2V, c_1 = 150 mM, c_2 = 050 mM as a function of the wall charge inside the pore. The wall charge was varied from -0.1 C/m^2 (top panel) to 0.2 C/m^2 (bottom panel) in 0.05 C/m^2 increments.

Chapter 6

Conclusions

This research effort was aimed at uncovering the factors that control the flux of ions through nanoporous materials and at developing the methods, tools, and capabilities required to build scientific insight and predictive capabilities for the analysis and design of materials and systems for membrane-based desalination of water. This work was carried out as a joint experimental and modeling effort involving researchers with expertise in membrane synthesis, structural and chemical analysis methods, atomistic-to-continuum simulation methods, and high performance parallel computing. This effort has laid the groundwork for future research into advanced desalination systems, experimental platforms for testing of novel membranes, and multiscale modeling methods for a wide range of non-equilibrium transport through nanoporous materials.

The experimental effort described in this report has provided significant insight into methods for surface modification and grafting of nanoporous polycarbonate materials, preparation of ion selective polyaniline materials, and a platform for experimental measurements of transport through desalination membranes. These studies have provided initial insight into the effects of surface charge and chemical modification of membrane materials on transport of concentration-driven and field-driven transport through ion exchange membranes. Thermal grafting of UV-ozone activated membranes was found to be an effective way to tune transport properties by altering the membrance surface characteristics. These studies will form the foundation for further studies on advanced membrane materials and the effect of chemical or structural membrane modifications.

The computational effort has resulted in a novel multiscale simulation framework for atomistic-to-continuum simulations of transport through nanopores. The model permits a wide range of representations of chemical and electronic detail, direct incorporation of experimental or computational parameters for transport or particle interactions, and fully coupled multiscale coupling of unbounded interactions such as electric field effects across the particle and continuum simulation domains. Parametric studies highlighted the role of membrane charges on ion selectivity and throughput. This model will continue to be developed and refined, with future applications expected across a wide range of simulations of nanopore transport properties.

References

[1] Swig: Simplified wrapper and interface generator. `http://www.swig.org`.

[2] H. Adalsteinsson, B. J. Debusschere, K. R. Long, and H. N. Najm. Components for atomistic-to-continuum multiscale modeling of flow in micro- and nanofluidic systems. *Scientific Computing*, 2009 (in press).

[3] P. Aimar. A study of selective electrodialysis and the possibilities offered by coupling with electrolysis. *Int. Chem. Eng.*

[4] O. Aktas and N. R. Aluru. A combined continuum/dsmc technique for multiscale analysis of microfluidic filters. *J. Comp. Phys.*, 178(2):342–372, MAY 2002.

[5] S. Al-Obaidani, E. Curcio, F. Macedonio, G. Di Profio, H. Al-Hinai, and E. Drioli. Potential of membrane distillation in seawater desalination: Thermal efficiency, sensitivity study and cost estimation. *Journal of Membrane Science*, 323(1):85–98, 2008.

[6] A. M. Alklaibi and N. Lior. Membrane-distillation desalination: Status and potential. *Desalination*, 171(2):111–131, 2005.

[7] T. W. Allen, S. Kuyucak, and S. H. Chung. Molecular dynamics estimates of ion diffusion in model hydrophobic and kcsa potassium channels. *Biophysical Chemistry*, 86(1):1 – 14, 31 2000.

[8] Y. Berdichevsky, J. Khandurina, A. Guttman, and Y. H. Lo. Uv/ozone modification of poly(dimethylsiloxane) microfluidic channels. *Sensors and Actuators B: Chemical*, 97(2-3):402–408, 2004.

[9] W. Bourcier, K. O'Brien, A. Sawvel, M. Johnson, K. Bettencourt, S. Letant, T. Felter, K. Langry, B. Wilson, J. Haslam, C. Schaldach, and D. Sopchak. Fy05 ldrd final report molecular engineering of electrodialysis membranes 03-erd-060. Technical Report UCRL-TR-219452, Lawrence Livermore National Laboratories, Livermore, CA, 2006.

[10] C. Cabassud, C. Burgaud, and J.-M. Espenan. Spring water treatment with ultrafiltration and stripping. *Desalination*, 137(1-3):123–131, 2001.

[11] J. Cervera, B. Schiedt, R. Neumann, S. Mafe, and P. Ramirez. Ionic conduction, rectification, and selectivity in single conical nanopores. *Journal of Chemical Physics*, 124(10):104706 – 1, MAR 2006.

[12] D. Chen, J. Lear, and B. Eisenberg. Permeation through an open channel: Poisson-nernst-planck theory of a synthetic ionic channel. *Biophysical Journal*, 72(1):97 – 116, 1997 1997.

[13] W. Chen. Surface modification and adhesion characteristics of polycarbonate films after graft copolymerization. *Journal of Polymer Science Part A: Polymer Chemistry*, 36(2):357–366, 1998.

[14] Y. J. Choi, T. Yamaguchi, and S. I. Nakao. A novel separation system using porous thermosensitive membranes. *Ind. Eng. Chem. Res.*, 39(7):2491–2495, 2000.

[15] B. Corry, M. Hoyles, T. W. Allen, M. Walker, S. Kuyucak, and S. H. Chung. Reservoir boundaries in brownian dynamics simulations of ion channels. *Biophysical Journal*, 82(4):1975 – 84, April, 2002.

[16] Ben Corry, Serdar Kuyucak, and Shin-Ho Chung. Tests of continuum theories as models of ion channels. ii. poisson-nernst-planck theory versus brownian dynamics. *Biophys. J.*, 78(5):2364–2381, May, 2000.

[17] P. S. Crozier, R. L. Rowley, N. B. Holladay, B. Henderson, and D. D. Busath. Molecular dynamics simulation of continuous current flow through a model biological membrane channel. *Phys. Rev. Lett.*, 86:2467–2470, 2001.

[18] E. L. Cussler. *Diffusion: Mass Transfer in Fluid Systems*. Cambridge University Press, Cambridge, 1997.

[19] G. Ducom, F. P. Puech, and C. Cabassud. Air sparging with flat sheet nanofiltration: a link between wall shear stresses and flux enhancement. *Desalination*, 145(1-3):97–102, 2002.

[20] J. Dzubiella, R. J. Allen, and J. P. Hansen. Electric field-controlled water permeation coupled to ion transport through a nanopore. *Journal of Chemical Physics*, 120(11):5001 – 4, Mar 2004.

[21] K. Efimenko, W. E. Wallace, and J. Genzer. Surface modification of sylgard-184 poly(dimethyl siloxane) networks by ultraviolet and ultraviolet/ozone treatment. *Journal of Colloid and Interface Science*, 254(2):306–315, 2002.

[22] B. Eisenberg. Proteins, channels and crowded ions. *Biophys. Chem.*, 100(1-3):507–517, 2003 2003.

[23] R. S. Eisenberg. Computing the field in proteins and channels. *Journal of Membrane Biology*, 150(1):1 – 25, 1996 1996.

[24] A. V. Finkelstein, D. N. Ivankov, and A. M. Dykhne. Energy barrier for an ion crossing an intra-membrane channel. *ArXiv Physics e-prints*, Dec 2006.

[25] N. G. Hadjiconstantinou. Hybrid atomistic-continuum formulations and the moving contact-line problem. *J. Comp. Phys.*, 154(2):245–265, SEP 1999.

[26] M. Heroux, R. Bartlett, V. Howle, R. Hoekstra, J. Hu, T. Kolda, R. Lehoucq, K. Long, R. Pawlowski, E. Phipps, A. Salinger, H. Thornquist, R. Tuminaro, J. Willenbring, A. Williams, and K. Stanley. An overview of the Trilinos Project. *ACM Trans. Math. Soft.*, 31(3), 2005.

[27] C. Ho, R. Qiao, J. B. Heng, A. Chatterjee, R. J. Timp, N. R. Aluru, and G. Timp. Electrolytic transport through a synthetic nanometer-diameter pore. *Proc. Natl. Acad. Sci.*, 102(30):10445–10450, JUL 2005.

[28] A. Hozumi, H. Inagaki, and T. Kameyama. The hydrophilization of polystyrene substrates by 172-nm vacuum ultraviolet light. *Journal of Colloid and Interface Science*, 278(2):383–392, 2004.

[29] Guoqing Hu and Dongqing Li. Multiscale phenomena in microfluidics and nanofluidics. *Chem. Eng. Sci.*, 62(13):3443–3454, 2007.

[30] Y. Ito, M. Inaba, D.J. Chung, and Y. Imanishi. Control of water permeation by ph and ionic strength through a porous membrane having poly(carboxylic acid) surface-grafted. *Macromolecules*, 25(26):7313–7316, 1992.

[31] H. Iwata, M. Oodate, Y. Uyama, H. Amemiya, and Y. Ikada. Preparation of temperature-sensitive membranes by graft polymerization onto a porous membrane. *Journal of Membrane Science*, 55(1-2):119–130, 1991.

[32] R. M. Jendrejack, J. J. de Pablo, and M. D. Graham. A method for multiscale simulation of flowing complex fluids. *J. Non-Newtonian Fluid Mech.*, 108(1/3):123–142, Dec 2002.

[33] K. R. Kull, M. L. Steen, and E. R. Fisher. Surface modification with nitrogen-containing plasmas to produce hydrophilic, low-fouling membranes. *Journal of Membrane Science*, 246(2):203–215, 2005.

[34] B. Leclercq, M. Sotton, A. Baszkin, and L. Ter-Minassian-Saraga. Surface modification of corona treated poly(ethylene terephthalate) film: adsorption and wettability studies. *Polymer*, 18(7):675–680, 1977.

[35] Sonia E. Letant, Charlene M. Schaldach, Mackenzie R. Johnson, April Sawvel, William L. Bourcier, and William D. Wilson. Pore conductivity control at the hundred-nanometer scale: An experimental and theoretical study. *Small*, 2(12):1504–1510, DEC 2006.

[36] S. C. Li, M. Hoyles, S. Kuyucak, and S. H. Chung. Brownian dynamics study of ion transport in the vestibule of membrane channels. *Biophysical Journal*, 74(1):37 – 47, January, 1998.

[37] K.R. Long. Sundance 2.1. `http://software.sandia.gov/sundance`.

[38] K.R. Long. Sundance 2.0 Tutorial. Technical Report SAND2004-4793, Sandia National Laboratories, 2004.

[39] Thomas Luxbacher. Electrokinetic characterization of flat sheet membranes by streaming current measurement. *Desalination*, 199(1-3):376–377, NOV 20 2006.

[40] James E. Miller. Review of water resources and desalination technologies. *Sandia Technical Report SAND2003-0800*, March 2003.

[41] S. Mirza. Reduction of energy consumption in process plants using nanofiltration and reverse osmosis. *Desalination*, 224(1-3):132–142, 2008.

[42] G. Moy, B. Corry, S. Kuyucak, and S. H. Chung. Tests of continuum theories as models of ion channels. i. poisson-boltzmann theory versus brownian dynamics. *Biophys. J.*, 78(5):2349–2363, May, 2000.

[43] US Bureau of Reclamation and Sandia National Laboratories. Desalination and Water Purification Technology Roadmap 2003. Technical report, US Bureau of Reclamation and Sandia National Laboratories, Denver, CO, 2003.

[44] D. K. Owens. The mechanism of corona and ultraviolet light-induced self-adhesion of poly(ethylene terephthalate) film. *Journal of Applied Polymer Science*, 19(12):3315–3326, 1975.

[45] Ho Bum Park, Benny D. Freeman, Zhong-Bio Zhang, Mehmet Sankir, and James E. McGrath. Highly chlorine-tolerant polymers for desalination. *Angew. Chem. Int. Ed. Engl.*, 47(32):6019–6024, 2008.

[46] Y. S. Park, Y. Ito, and Y. Imanishi. Permeation control through porous membranes immobilized with thermosensitive polymer. *Langmuir*, 14(4):910–914, 1998.

[47] E. E. Polymeropoulos and J. Brickmann. Molecular dynamics of ion transport through transmembrane model channels. *Annual Review of Biophysics and Bioengineering*, (0101):315 – 330, 1985.

[48] R.F. Probstein. *Physicochemical Hydrodynamics: An Introduction*. John Wiley and Sons, Inc., New York, 2nd edition, 1994.

[49] A. V. R. Reddy, J. J. Trivedi, C. V. Devmurari, D. J. Mohan, P. Singh, A. Rao, S. V. Joshi, and P. K. Ghosh. Fouling resistant membranes in desalination and water recovery. *Desalination*, 183(1-3):301–306, 2005.

[50] Liqing Ren, D. Sinton, and Dongqing Li. Numerical simulation of microfluidic injection processes in crossing microchannels. *J. Micromech. Microeng.*, 13(5):739–747, 2003.

[51] M. D. Romero-Sánchez, M. Mercedes Pastor-Blas, and J. M. Martín-Martínez. Treatment of a styrene-butadiene-styrene rubber with corona discharge to improve the adhesion to polyurethane adhesive. *International Journal of Adhesion and Adhesives*, 23(1):49–57, 2003.

[52] B. Roux and M. Karplus. Molecular dynamics simulations of the gramicidin channel. *Annu. Rev. Biophys. Biomol. Struct.*, 23:731–761, 1994.

[53] H.A. Schwarz. Über einige abbildungsaufgaben. *Journal für Reine und Angewandte Mathematik*, 70:105–120, 1896.

[54] C. I. Siettos, M. D. Graham, and I. G. Kevrekidis. Coarse brownian dynamics for nematic liquid crystals: bifurcation, projective integration, and control via stochastic simulation. *J. Chem. Phys.*, 118(22):10149 – 56, JUN 2003.

[55] Z. Siwy and A. Fulinski. A nanodevice for rectification and pumping ions. *American Journal of Physics*, 72(5):567 – 574, MAY 2004.

[56] M. L. Steen, L. Hymas, E. D. Havey, N. E. Capps, D. G. Castner, and E. R. Fisher. Low temperature plasma treatment of asymmetric polysulfone membranes for permanent hydrophilic surface modification. *Journal of Membrane Science*, 188(1):97–114, 2001.

[57] B. J. A. Tarboush, D. Rana, T. Matsuura, H. A. Arafat, and R. M. Narbaitz. Preparation of thin-film-composite polyamide membranes for desalination using novel hydrophilic surface modifying macromolecules. *Journal of Membrane Science*, In Press.

[58] Y. Tsunoda and M. Kato. Compact apparatus for sea water desalination by electrodialysis using ion exchange membranes. *Desalination*, 3(1):66–81, 1967.

[59] M. Ulbricht and G. Belfort. Surface modification of ultrafiltration membranes by low temperature plasma ii. graft polymerization onto polyacrylonitrile and polysulfone. *Journal of Membrane Science*, 111(2):193–215, 1996.

[60] W. F. van Gunsteren, H. J. C. Berendsen, and J. A. C. Rullmann. Stochastic dynamics for molecules with constraints-brownian dynamics of n-alkanes. *Mol.Phys.*, 44(1):69–95, 1981.

[61] J. Wang and P. Somasundaran. Reversible conformational behavior of poly(acrylic acid) lb film with changes in ph, ionic strength and time. *Colloids and Surfaces A: Physicochemical and Engineering Aspects*, 273(1-3):63–69, 2006.

[62] A. Warshel and M. Levitt. Theoretical studies of enzymic reactions: Dielectric, electrostatic and steric stabilization of the carbonium ion in the reaction of lysozyme. *J. Mol. Biol.*, 103(2):227–249, May 1976.

[63] R. Xie, L.-Y. Chu, W.-M. Chen, W. Xiao, H.-D. Wang, and J.-B. Qu. Characterization of microstructure of poly(n-isopropylacrylamide)-grafted polycarbonate track-etched membranes prepared by plasma-graft pore-filling polymerization. *Journal of Membrane Science*, 258(1-2):157–166, 2005.

[64] A. Zach-Maor, R. Semiat, A. Rahardianto, Y. Cohen, S. Wilson, and S. R. Gray. Diagnostic analysis of ro desalting treated wastewater. *Desalination*, 230(1-3):239–247, 2008.

[65] H. Zhang and Y. Ito. ph control of transport through a porous membrane self-assembled with a poly(acrylic acid) loop brush. *Langmuir*, 17(26):8336–8340, 2001.

DISTRIBUTION:

	MS	,
		,
1	MS 0899	Technical Library, 8944 (electronic)

Sandia National Laboratories